Nano-engineered pinning centres in YBCO superconducting films

Crisan, Ioan; Dang, Van-Son; Mikheenko, P.

DOI:
10.1016/j.physc.2016.06.011

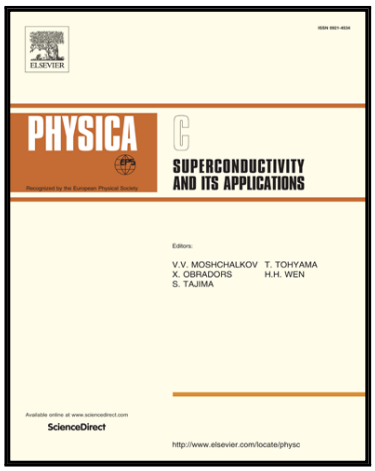

Nano-engineered pinning centres in YBCO superconducting films

A. Crisan , V.S. Dang , P. Mikheenko

PII: S0921-4534(16)30078-8
DOI: 10.1016/j.physc.2016.06.011
Reference: PHYSC 1253041

To appear in: *Physica C: Superconductivity and its applications*

Received date: 10 January 2016
Revised date: 9 June 2016
Accepted date: 10 June 2016

Please cite this article as: A. Crisan , V.S. Dang , P. Mikheenko , Nano-engineered pinning centres in YBCO superconducting films, *Physica C: Superconductivity and its applications* (2016), doi: 10.1016/j.physc.2016.06.011

Highlights

- Power applications of YBCO films/coated conductors in technological relevant magnetic fields requires nano-engineered pinning centre
- Three approaches have been proposed: substrate decoration, quasi-multilayers, and targets with secondary phase nano-inclusions.
- Combination of all three approaches greatly increased critical current in YBCO films
- Bulk pinning force, pinning potential, and critical current density are estimated and discussed in relation with the type and strength of pinning centres related to the defects evidenced by Transmission Electron Microscopy

Nano-engineered pinning centres in YBCO superconducting films

A.Crisan[1,2,*], V.S. Dang[2,3], P. Mikheenko[2,4]

[1] *National Institute for Materials Physics Bucharest, 105 bis Atomistilor Str., 077125 Magurele, Romania*

[2] *School of Metallurgy and Materials, University of Birmingham, Edgbaston, B15 2TT Birmingham, UK*

[3] *Nano and Energy Center, VNU Hanoi University of Science, 334 Nguyen Trai, Thanh Xuan, Hanoi, Vietnam*

[4] *Department of Physics, University of Oslo, P.O. Box 1048 Blindern, N-0316 Oslo, Norway*

[*]Corresponding author: adrian.crisan@infim.ro; acrisan652@gmail.com

Abstract

For practical applications of superconducting materials in applied magnetic fields, artificial pinning centres in addition to natural ones are required to oppose the Lorentz force. These pinning centres are actually various types of defects in the superconductor matrix. The pinning centres can be categorised on their dimension (volume, surface or point) and on their character (normal cores or $\Delta\kappa$ cores). Different samples have been produced by Pulsed Laser Deposition, with various thicknesses, temperatures and nanostructured additions to the superconducting matrix. They have been characterized by SQUID Magnetic Properties Measurement System and Physical Properties Measurement System, as well as by Transmission Electron Microscopy (TEM). Correlations between pinning architecture, TEM images, and critical currents at various fields and field orientations will be shown for a large number of $YBa_2Cu_3O_x$ films with various types and architectures of artificial pinning centres.

Keywords: YBCO films, pinning centres, pinning potential, critical current, critical current anisotropy

I. Introduction

Quite soon after the discovery of the high-temperature superconductor (HTS) $YBa_2Cu_3O_7$ (YBCO) with critical temperature above liquid nitrogen in 1987 [1], a world-wide research effort led to the demonstration of a wide range of applications, based on both HTS thin films (cryo-electronic devices) and on HTS wires, tapes and conductors (power devices), with the potential of making a huge impact on science, technology, sustainable growth and quality of life. However, a few serious problems are still remaining to be solved. The critical current is usually strongly depressed by magnetic fields, especially at higher temperatures, due to Lorentz forces and thermal fluctuations that lead to the movement of magnetic flux lines (vortices). Fortunately, such movement can be suppressed by sufficiently strong pinning centres in the HTS material. So, engineering of artificial pinning centres and fundamental studies regarding their effects on the vortex dynamics and other superconducting (SC) properties are of great importance for science and technology of HTS, and, consequently, for the market penetration of HTS devices.

In HTS, critical current density (J_c) is determined by the pinning of flux lines by defects in the crystal structure [2] such as dislocations, grain and twin boundaries, non-superconducting precipitates. Although the natural growth-induced defect density in epitaxial thin films is already much higher than in bulk material, allowing critical current density at 77 K of about 10^6 A/cm^2, their density and strength is often too small to maintain sufficiently high critical currents in a technically relevant magnetic field [3]. Many groups demonstrated that an improvement of J_c can be obtained by the introduction of artificial defects acting as pinning centres. A number of different methods have been successfully used to enhance J_c in thin films in which heavy-ion and neutron irradiation proved to be very efficient, but less suitable than alternative routes for practical applications [4, 5, 6]. Another successful approach was through doping with various elements and compounds, like Zn, $BaZrO_3$, LiF, Ca, etc., [7-11], that proved to be useful also for polycrystalline superconductors [12, 13]. In superconducting films films, regular arrays of (sub)-micron defects (holes, metallic and magnetic dots) fabricated through photolithography were shown to pin the magnetic flux lines [14, 15].

The earliest cost-effective method used for introducing artificial pinning centres in superconducting films was the so-called substrate decoration approach [16] that consists of growing nano-scale islands (nano-dots) of certain non-superconducting materials on the substrate prior to the deposition of the superconducting thin film. Later on, two other approaches proved to be successful in the nanotechnology of pinning centres: building up a

layered distribution of a second phase using multilayer deposition (quasi-superlattices) [17], and, secondly, by the distribution of secondary phases of nanoscale grain dimensions in the film achieved by a modified target composition [18]. Several materials have now been used as nano-scale pinning centres. In the case of substrate decoration, Ag nano-dots were first used for Tl-based superconducting films [16, 19-20] and then for YBCO grown by Pulsed Laser Deposition (PLD) [21], followed by MgO [22], Y_2O_3 [23, 24], Ce_2O_3 [25], Ir [26], Au and Pd [27]. For the quasi-superlattices (quasi-multilayers) approach the nano-dot materials used till now are Y_2BaCuO_5 [17], Y_2O_3 [28, 29], yttria stabilized zirconia (YSZ) [30], Ba*TM*O_3 (*TM* = transition metal = Ir, Ti, Zr, Hf) [31], transition metals [32], Ag, Au, Pd and non-superconducting YBCO [27]. In the case of compositionally changed targets, $BaZrO_3$ (BZO) has been used most commonly as an impurity addition to $YBa_2Cu_3O_{7-\delta}$ targets [18, 34, 35]. More recently, $BaNb_2O_6$ and $BaSnO_3$ have been added as impurities to $ErBa_2Cu_3O_{7-\delta}$ targets [36, 37], while $BaSnO_3$ [37], $Gd_2Ba_4CuWO_{12}$ [38, 39], RE_3TaO_7 (*RE* = rare earth = Er, Gd, Yb) [40], YBa_2NbO_6 [41] and YBa_2TaO_6 [42] were added to YBCO targets.

Here we will review some of the results obtained in YBCO films by Ag nanodots substrate decoration, quasi-multilayer approach, use of targets with BZO nano-inclusions, as well as combinations of different techniques that led to synergetic pinning centres.

II. Experimental, measurements and data analysis

The films were grown by Pulsed Laser Deposition (PLD) on $SrTiO_3$ (STO) single-crystal substrates using a KrF excimer laser with 248 nm wavelength with pulse duration of 30 ns, repetition rate of 3-8 Hz, laser energy density of 0.7-1.7 J/cm^2, laser energy between 240 and 266 mJ, and target–substrate distance of 5 - 6 cm, the laser having a scanning beam. Deposition chamber and an image of the PLD plume inside the chamber are shown in Figure 1. This method consumes the target material gradually and homogeneously and does not require frequent and intermediate polishing of the target, which makes the technique potentially suitable for the large-scale production of superconducting coated conductors. Substrate temperatures were either 780 ^oC or 800 ^oC and the oxygen partial pressure during deposition was 450 mTorr. After the deposition, the films were cooled down in partial oxygen atmosphere of 450 Torr at the rate of 8^o C/min. For YBCO films with Ag substrate decoration, the same conditions for YBCO growth have been used. Prior to YBCO deposition, Ag nanodots were optimised and grown, also by PLD at a substrate temperature of 400^o C in vacuum. For Ag/YBCO quasi-superlattices, the same conditions for YBCO and Ag were used, by alternating YBCO layers and Ag quasi-layers several times. The same

growth conditions were used for YBCO/PBCO quasi-multilayers. When a YBCO target with 4% BZO nanoinclusions was used, the higher temperature of 800 ^{o}C combined with a lower repetition rate of 3 Hz led to better results.

To make small bridges of micrometres sizes for transport measurements, samples patterning using acid etching were employed. After cleaning with Acetone and 2-Isopropanol, the sample was placed on a speed controllable spinner, and, while rotating with a speed of 4000 rpm, 2 or 3 photoresist S1818 droplets were applied on the surface of the sample which continued to rotate for 30 seconds to a minute. The sample then was baked for a few minutes at a temperature of 120^{o} C before being exposed to an UV400 Exposure Optics (for 365nm and 405nm exposure) UV source through a mask, designed to form 4 bridges with lateral size from 5μm to 50μm, using a Karl Suss MJB3 Mask Aligner. The exposed sample then was developed in Microsposit MF-319 developer for a few minutes. Diluted Nitric acid 0.1% was used to etch the developed samples. The sample was immersed in the diluted acid for several minutes, depending on the thickness of the film. Normally, a 1μm thick-film sample will take about 10 minutes etching. The etching time is not growing linearly with the thickness, the thicker the film, the more difficult is to etch the sample. Less than 1μm thick film is easily and quickly etched, but several microns thick films were also etched successfully. The etched samples were then cleaned by acetone again to remove the photoresist layers and remaining acid in an ultrasonic bath. In some cases, the smallest bridge (about 5-6 μm) was broken due to ultrasonic vibration or over-etching. Figure 2 show typical views of patterned sample with 4 bridges of different widths, and with the smallest surviving bridge.

To become transparent for electrons, a specimen needs to be thinned to less than 100 nm, which was done by Focused Ion Beam technique using the Quanta 3D FEG system with dual beam which combines a scanning electron microscope (SEM) and focused ion beam (FIB). The whole sample surface was first coated with a thin gold layer. A selected area of interest on the sample was then coated with a tungsten (W) protective layer. A large trench on alternating sides of the protective layer was then milled and the membrane thinned below 2 μm. The thin sample was cut, lifted out and transferred to a TEM grid with an omniprobe. The final step was thinning the sample to the required thickness. The sequence of step is shown in Figure 3.

The surface morphology of the films was characterised by Scanning Electron Microscopy (SEM). The surface of the YBCO films, as well as of doped YBCO films, does

not have a smooth surface, containing pores and precipitates. Knowing the surface characteristics is one of the key points to study the pinning mechanism of the YBCO films. The Jeol JSM-7000F SEM, was used in this work, with different magnifications. Most of measurements were taken under the accelerating voltage of 20 kV and probe current of about 120 μA. Atomic force microscopy (AFM) is commonly used in investigating sample surfaces at the nanoscale, in addition to SEM. The Veeco Multimode AFM was used in this project to analyse topography of nano-particles (Ag, PBCO) grown on substrates for the substrate decoration approach. For higher resolution images necessary for our substrates decorated with nano-dots, tapping mode was used, with a super-sharp tip (smaller than 10 nm diameter, normally 1 nm). The tapping mode means the tip is approached very close to contact with the sample surface and then lifted off the surface to avoid dragging the tip across the sample surface. The cantilever is excited in vibration with a frequency near to the resonant frequency of the tip. The vibrated cantilever is maintained during tapping operation. The images then were re-analysed by WSxM 5.0 free software and Imagetool software. Nano-engineered defects in the films were analysed in cross-section using Transmission Electron Microscopy (TEM). The cross section images of the thinned samples were taken by a Jeol JEM 2100 TEM using lanthanum hexaboride (LaB_6) crystal thermionic electron source. The TEM was operated at 200 kV and magnification up to 200,000 times. The Tecnai F20 TEM using field emission electron source was also used in the project. Due to the field emitter gun the Tecnai F20 was equipped with Scanning Transmission Electron Microscopy (STEM) and Oxford EDS system. High resolution images can be obtained by the Tecnai F20 (HRTEM) and element mapping was also analysed in the STEM mode by the EDS system. Bright field image with (001) zone axis was selected in most of the TEM images.

Critical temperature, and, respectively, critical current density and bulk pinning force were determined from AC susceptibility, and, respectively, from DC magnetization loops using a *Quantum Design* Magnetic Properties Measurement System MPMS-XL, in fields $\mu_0 H_{DC}$ up to 4 T. Frequency-dependent J_c (77.3 K, $\mu_0 H_{DC}$), and, consequently, average pinning potentials of the pinning centres were determined from the AC field dependencies of the out-of-phase susceptibility χ" measured on a *Quantum Design* Physical Properties Measurement System PPMS in $\mu_0 H_{DC}$ up to 6 T, AC field amplitude h_{ac} up to 10 Oe, and AC field frequency f between 47 and 9997 Hz.

To determine T_c, the temperature dependence of $\chi=\chi'-i\chi''$ was registered. Normally, the minimum excitation field of the MPMS system of 0.05 Oe was used to determine T_c; a higher excitation field results in an underestimated T_c due to a higher probing current. In fact, both χ' and χ'' depend not only on temperature and AC amplitude, but also on AC frequency (especially in higher fields where thermally-activated flux creep is time-dependent).

Critical current density (J_c) of a thin film sample can be easily estimated from the DC magnetisation loops using the critical state model (Bean model) that assumes that the current flowing in the sample is either the critical current J_c or zero. *Quantum Design* MPMS XL system was used to measure magnetisation loops of all samples. The film surface (superconducting a-b planes) is normal to the applied magnetic field. Most of samples were 5 x 5 mm and in this case, J_c was calculated as

$$J_c = \frac{6m}{a^3 d} \qquad (1)$$

where m is the irreversible magnetic moment, or half of the width of the magnetisation loop. In some cases, samples were accidently broken while taking out from the heater, and the broken samples were polished in rectangular shape with dimensions a and b (a < b). For such rectangular samples, J_c was estimated from

$$J_c = \frac{4m}{a^2 bd(1-\frac{a}{3b})}. \qquad (2)$$

where d is film thickness. This is a frequently used equation ([43, 44], in CGS units), derived from a critical state model.

Apart from critical current density, from DC magnetization loops one can also determine the bulk (total) pinning force $F_p=B\text{x}J_c$. In order to understand pinning mechanisms, the Dew-Hughes [45] model of flux pinning mechanisms in type II superconductors was used to analyze our data for pure YBCO films and Ag/YBCO multilayer films. According to Dew-Hughes, the pinning centres are of two types: "$\Delta\kappa$ pinning" due to small differences in the Ginzburg constant κ, arising from changes in the normal state resistivity due to composition fluctuations, or non-uniform distributions of dislocations and "normal pinning" due to non superconducting particles, which may be normal metal, insulator or void. In additions, pinning centres can be point pins, surface pins and volume pins, in relation with the number

of their respective dimensions (1,2 or 3) that are large compared with the inter-flux-line spacing d $\left(=1.07(\Phi_0 / B)^{0.5}\right)$ where Φ_0 denotes the flux quanta. In Dew-Hughes model, the field dependence of the normalised pinning force F is $F_p/F_{pmax} = h^p(1-h^q)$ where $h = B/B_{irr}$, where B_{irr} is the irreversibility field, taken at the 10^3 A/cm^2 criterion, while p and q values depend on the types of pinning centres. The values of p and q for the pinning centres of interest are given by Dew-Hughes, and will be addressed below. When there are several types of pinning centres in the same sample, the normalised pinning force can be described by:

$$F = Ah^{p1}(1-h)^{q1} + Bh^{p2}(1-h)^{q2} + Ch^{p3}(1-h)^{q3} + \cdots \quad (3)$$

The constants *A*, *B*, *C*, etc. are calculated in Ref. 43 for the case of "classical" low temperature type II superconductors. Here we treat them only as fitting parameters, with only condition that *A*, *B*, *C*, etc. values to provide that the maximum of F_p/F_{pmax} to be 1, where there is a maximum, in the case of only one type of pinning. More clearly, for example, in the case of normal surface pinning, p=0.5, q=2, F_p/F_{pmax} has a maximum for h=0.2, and, for $F_p(h=0.2)/F_{pmax}$, to be 1, the condition is that the constant C should be equal to 3.5. In Table 1 are presented the values for p and q, as well as the maximum values for the constants *A*, *B*, *C*, etc. for various types of pinning centres. We have fitted using try-and-error approach the experimental data taking into account not more than 3 types of pinning centres. It is worth noting that the most significant error comes from the estimation of irreversibility field.

The critical current density can also be calculated from AC susceptibility while a DC field is applied to the sample (or zero DC applied field at temperatures close to T_c). The dependence of J_c on DC field, temperature and AC frequency can be determined from AC susceptibility measurements. By installing the AC Measurement System (ACMS) option of the Quantum Design Physical Properties Measurement System (PPMS), the dependence of χ' and χ'' on AC frequency and DC applied field, at fixed temperatures, could be measured. The fundamental frequency components of the AC susceptibility have clear physical meanings: χ' measures the shielding effect of super-currents and χ'' measures the hysteretic energy loss per cycle per unit volume. From calculations of Brandt [46] on the flux penetration in superconductors with one dimension much smaller than the other two (disks, squares, stripes) in a perpendicular configuration (suitable for thin films with magnetic field perpendicular to the film surface), it was shown that the position h^* of the maximum in $\chi''(h_{ac})$ is related to the critical current density by the equation

$$J_c = \frac{h^*}{\alpha d}, \tag{4}$$

where d is the film thickness and α is a constant between 0.8 and 0.9 that depends slightly on the geometry. An example of such frequency-dependent χ"(h_{ac}) measured curves is shown in Figure 4, for a PBCO/YBCO quasi-multilayer (2 quasi-layers of $PrBa_2Cu_3O_7$ nano-dots interspaced with two 565 nm-thick YBCO layers) at 77.3 K and in 4 T DC field. From the frequency (time) dependence of critical current density one can estimate the pinning potential. Our attempts to describe the experimental data by the power-law current density dependence of the pinning potential from the weak collective pinning theory [47], by the linear Anderson-Kim (AK) model [48] or by a modified AK model [49] were unsuccessful. Instead, as can be seen in fig. 5, our data are very well described by a straight line in a double logarithmic plot:

$$\ln J_c = a - b \ln\left(\frac{f_0}{f}\right). \tag{5}$$

where f_0 is a macroscopic attempt frequency of about 10^6 Hz [50]. The above dependence is consistent with a logarithmic dependence of the effective pinning potential on the current density, as proposed by Zeldov and co-workers based on magneto-resistivity [51] and current-voltage characteristics [52] measurements of YBCO thin films:

$$U_{eff} = U_0 \ln\left(\frac{J^*}{J}\right), \tag{6}$$

where J^* is a "critical current density" at which the effective pinning potential U_{eff} approaches zero (cross-over between flux creep and flux flow). It can be shown that, by using eq. (6) for the current dependence of effective pinning potential, U_0 can be related to the slope b in eq. (5) of our experimental data (complete derivation is given in Ref. 34):

$$U_0 = k_B T\left(1 + \frac{1}{b}\right). \tag{7}$$

To estimate the anisotropy of critical current in respect to the angle made with the surface of the film with the applied magnetic field, and to gain a deeper insight of the type and strength of artificial pinning centres, the angular-dependent critical current density transport measurements were performed. The transport measurements were carried out using

the PPMS system with AC Electronic Transport with rotator option inserted. The patterned sample was connected with the sample holder by indium solder through gold wires. The angular range was from -10 to 370^{o} and a maximum applied field of 6 T was used. With transport measurement as described in Figure 6, not only the angle between applied field and the c-axis of the sample (θ) can be changed but also applied field (B) and temperature (T) can be controlled, so $J_c(\theta, B, T)$ was determined. Depending on the size of the bridges, various voltage criteria down to 1 μV/cm were used.

III. Results and Discussion

For the case of ***substrate decoration***, the optimum conditions in which Ag nano-particles uniformly distributes on the STO substrate and produced the largest improvement of critical current was successfully found to be deposition temperature of 400 ^{o}C and 15 laser pulses on the Ag target. Ag nano-particles are uniformly distributed on the STO substrate, with an average diameter of 13 nm and average height of 3.4 nm. An example of AFM image of Ag nano-dots is shown in Figure 7. The same temperature and number of laser pulses on PBCO target led to the growth of a high number density of PBCO nano-dots, the substrate being almost entirely covered. In case of Au nano-particles, the optimum growth conditions were found to be deposition temperature of 780 ^{o}C and 25 laser pulses, which led to an average diameter of 12.3 nm, close to the case of optimum decoration with Ag particles. For higher number of laser pulses up to 75, Au nano-particles are still well separated. Overall, standing alone or in combination with the quasi-multilayer approach or/and use of BZO-doped YBCO target, the best results were obtained from Ag nanodots. The increase in critical current density for substrate decoration is noticeable, 2-3 times in lower field, and one order of magnitude only for fields over 2-3 T, as can be seen in Figure 8. The most significant effect of Ag (and Au) substrate decoration proved to be the *columnar growth of YBCO*, leading to a high density of surface normal pinning centres [53, 54], and to the possibility of growing much thicker films (up to 5-6 μm in our experiments) without the usual drastic reduction in J_c with film thickness. This effect allows us to greatly improve the critical current (which is actually the parameter of interest for power applications) simply by growing much thicker films that those usually reported to have record critical current densities (and ***not*** record critical currents). Figure 9 show cross-sectional AFM images (on the side of

freshly-broken specimens) on the YBCO/STO interface for YBCO films grown on bare (for comparison) and Ag and Au decorated substrates.

It is known from literature that usually J_c rapidly decreases with increasing of film thickness. In order to obtain high critical current per cm-width (I_c), ideally over 1000 A/cm-width in self-field and hundreds A/cm-width in fields of few T, increasing the film thickness without decreasing too much J_c is required. Taking into account the catalytic effect of silver that allows the growth of thicker films on Ag nano-dots decorated substrates, the next YBCO films grown and studied had the ***quasi-multilayer architecture***, being composed of quasi-layers of Ag (grown by 15 laser pulses on Ag target) interspaced with layers of YBCO with a certain thickness, the sequence repeating several times (N). These samples are denoted in figures by (15Ag/mYBCO)xN, where m is the thickness of each of YBCO layers and N is the number of deposition sequences. Figure 10 shows the field dependence of critical current density at 77 K (in comparison with a pure YBCO film of 2 μm-thickness), and of critical current at 70 K of a few quasi-multilayers composed of Ag quasi-layers interspaced with 1.5 μm-thick YBCO layers,. It can be seen that, except for the 6 μm-thick quasi-multilayer in fields below 1.5 T, the quasi-multilayer architecture leads to higher J_c in comparison with both pure YBCO and with the substrate-decorated film (N=1). As for the critical current at 70 K, this approach increases I_c several times at low fields, and by an order of magnitude at higher fields.

The use of ***targets with nano-inclusions*** (like BZO, the first case studied) for artificial pinning centres is the third cost-effective method used in the nanotechnology of pinning centres [18]. More recently, it was shown [55] that through deposition temperature and laser pulses frequency the type of defects (*c*-axis correlated columnar defects, splayed columnar defects, and randomly distributed nanoparticles) can be controlled, due to difference in growth kinetics. For this study we have used an YBCO target containing 4% BZO nanoinclusions with nanometer-sized grains prepared by a citrate-gel method [56]. Unlike the previous substrate decorated samples and quasi-multilayers in which optimum deposition conditions, with our equipment, proved to be a deposition temperature of 780 ^{o}C and a laser pulses frequency of 5-8 Hz, in the case of the nano-crystalline BZO-doped YBCO target we found that for best samples (high and sharp T_c and high J_c in applied fields), the optimum condition to deposit BZO-doped YBCO film is at a high substrate temperature of 800 ^{o}C and low laser frequency of 3 Hz. Figure 11 shows the field dependence of J_c at 65 K of BZO-doped YBCO film deposited at 780^{o}C and 8 Hz and at 800^{o} C and 3 Hz in comparison with J_c

of YBCO film grown at 780^{o} C and 8 Hz. The reason for the very different behaviour of the two BZO-doped films is that by increasing deposition from 780 to 800^{o} C and lowering laser frequency from 8 Hz to 3 Hz, the formation of the BZO in the YBCO matrix changed from nano-particles to columnar structure parallel to the *c*-axis of the film (and DC magnetization loops are measured with field in the same direction, so columns are more effective pinning centres in this case). This reason was revealed from TEM images, shown later on. With increasing thickness of BZO-doped YBCO films, a decrease in the quality of the films in terms of critical current density and critical temperature was observed, which was not the case for the Ag/YBCO quasi-multilayers, as discussed above. This is another proof of the beneficial influence of Ag in YBCO films.

For this reason, the next logical step was to incorporate the use of nano-crystalline BZO-doped target with Ag substrate decoration and Ag/BZO-dopedYBCO quasi-multilayer approach (an ***integrated nanotechnology of pinning centres***) to create ***synergetic pinning centres*** in thick (up to 5-6 μm) YBCO films [57,58]. Ag nanodots substrate decoration has a visible positive influence on J_c of BZO-doped YBCO films of moderate thickness, as can be seen in Figure 12. For much thicker films, the positive effect of Ag substrate decoration is lost, hence the need for Ag/BZO-dopedYBCO quasi-multilayer approach. Figure 13 shows the positive effect of an intermediate Ag quasi-layer in the middle of a 2 μm thick BZO-doped YBCO film. Figure 14 presents the field dependence of J_c of a 2μm-thick Ag/BZO-doped YBCO single layer, a 6μm-thick Ag/BZO-doped YBCO trilayer and a 2.0 μm-thick pure YBCO single layer at 77.3 K. The huge increase in comparison with pure YBCO film is obvious. It seems unfair to compare J_c of a thick film with that of a thin film; however, it is clearly seen that J_c of the 6 μm multilayer is not 3 times smaller than that of the thinner 2 μm single layer at both temperatures of 65 K and 77.3 K. By using a multilayer architecture, J_c of a thick film still remains high enough such that the total critical current per cm-width of a thick multilayer film is much higher than a thin single layer. The critical current per cm-width of the 6 μm multilayer film is shown in Figure 15, in which one can estimate that critical currents per cm-width are about 1700 A/cm and 800 A/cm at 65 K and 77.3 K, respectively, in self-field, and 1080 A/cm and 330 A/cm at 65 K and 77.3 K, respectively, in 0.5 T. It can be seen that at 65 K, a temperature easily attainable by pumping liquid nitrogen (or by simple cryo-coolers) hundreds of A can be transported without loss in such nano-engineered thick films.

Regarding the ***bulk pinning force***, our experiments and data analysis of a large number of samples, having various types of architectures and materials for nano-dots, showed that in all cases the dominant pinning mechanism, at least at 77 K, is surface normal. Figure 16 shows several examples of experimental data, fitted with the procedure described before. In (a) is a pure YBCO film; in (b) a Ag/YBCO quasi-multilayer; (c) 15Ag/BZO-doped YBCO; and (d) a PBCO/YBCO quasi-multilayer (again, PBCO nanodots were grown using 15 laser shots on PBCO target). From fitting, we could estimate that in (a) there is 79.4% normal surface (C= 2.87) and 20.6% normal point pinning (E=1.47); in (b) 85.3% normal surface (C= 3.11) 7.5% Δκ surface (D=0.42) and 7.2% normal point pinning (E= 0.51); in (c) 61.2% normal point (E= 4.26) and 38.8% normal surface pinning (C= 1.40), coefficients C, D, and E being the ones described in table 1.

The average ***pinning potentials*** determined, for various types of nanoengineered YBCO samples, from frequency-dependent AC susceptibility measurements, show some interesting features, depending on nature and architecture of nano-dots. Below we will show 3 examples. The first one regards 1.27 μm - thick films ablated from a nano-crystalline $YBa_2Cu_3O_{7-\delta}$ (YBCO) target doped with 4 wt.% $BaZrO_3$ (BZO), nYBCO/BZO, and from a commercial micro-crystalline pure YBCO target. Figure 17 (left-hand side) shows the frequency dependence of J_c, J_c vs. $\ln(f_0/f)$, where f_0 is a macroscopic attempt frequency of about 10^6 Hz as discussed in the previous chapter, at 77.3 K and several DC fields in the two films, calculated from equation (4) with h^* determined experimentally from the $\chi''(h_{ac})$ curves and $\alpha = 0.8$, while the right-hand side shows the values of pinning potential at various DC fields, as calculated from Eq. (7). It should be noted that the experimental window in which J_c can be estimated in this way is limited by the experimental range of both AC field amplitudes and frequencies. It can be seen that the average pinning potential of nYBCO/BZO film are higher and, even if the increase does not seem impressive, the exponential dependence of dissipation (Arrhenius-type) implies a much lower dissipation caused by thermally activated flux creep in the thick film with artificial pinning centres induced by BZO, hence the much higher critical current density in the BZO-doped nanostructured film. Quite different is the case of films grown on STO substrates decorated with $LaNiO_3$ nano-dots. Figure 18 shows the frequency dependence of J_c for a 1.6 μm – thick film grown on STO substrate decorated with $LaNiO_3$ nano-dots grown by 10 laser pulses (LNO10/YBCO) at 200 °C and 10 mTorr oxygen pressure, in comparison with a 0.96 μm – thick film grown on bare substrate, in DC magnetic fields of 3, 4 and 5 T. The values of the pinning potential U_0

calculated, in Kelvin (k_B = 1), from the slopes in figure 18 using eq. (7) are 406.2 K and 363.6 K in 3 T; 255 K and 247.2 K in 4 T, and 150.2 K and 150.9 K in 5 T for LNO10/YBCO and reference film, respectively. The difference in U_0 between the two films is very small and practically none in 5 T, the two straight lines in the double logarithmic plot in Figure 18, for each field, being almost parallel, unlike the case of $BaZrO_3$-doped films, in which U_0 is significantly higher. This means that the pinning potential of the defects induced by LNO substrate decoration is almost the same as that of the defects that occur naturally in YBCO films, while the increase in the critical current density is due to a larger number of such defects, the most likely candidate being the dislocations [59]. This situation is probably similar to the increase of dislocation density by substrate decoration with Y_2O_3 [60]. The third example is that of thick quasi-multilayers composed of incomplete layers of $PrBa_2Cu_3O_x$ (PrBCO nanodots) and layers of $YBa_2Cu_3O_{7-\delta}$ (YBCO). The number of such sequences was between 2 and 6, with the thickness of individual YBCO layers between 565 and 885 nm, and total thickness between 1.13 and 5.31 μm. Frequency-dependent AC susceptibility measurements were performed on three different quasi-multilayers: the first was composed of two quasi-layers of PrBCO nanodots grown in vacuum at a substrate temperature of 450 °C by 20 laser pulses interspersed with two layers (565 nm thick each) of YBCO grown at 782 °C in 450 mTorr oxygen partial pressure, having a total thickness of 1.13 μm (denoted thereafter as (20Pr/565nmY)x2); the second was composed of three quasi-layers of PrBCO nanodots grown by 15 laser pulses and three layers (843 nm thick each) of YBCO, all grown at 780 °C in 450 mTorr oxygen partial pressure, having a total thickness of 2.53 μm (denoted thereafter as (15Pr/843nmY)x3); and the third architecture was composed of six quasi-layers of PrBCO nanodots grown by 15 laser pulses and six layers (885 nm thick each) of YBCO, grown in the same conditions as the second type, having a total thickness of 5.31 μm (denoted thereafter as (15Pr/885nmY)x6). Frequency dependence of J_c of the above-mentioned quasi-multilayers is shown in Figure 19, where the pure YBCO sample for comparison is the same as in Figure 18 (a 0.96 μm – thick film grown on bare substrate). As can be seen from Fig. 19, in 4 and 5 T the critical current densities of all three quasi-multilayers are higher than that of the reference sample, while in 3 T only the 1.13 μm (20Pr/565nmY)x2 film shows an improvement (note that J_c is expected to decrease with thickness). On the other hand, from the slopes of J_c vs. $\ln(f_0/f)$ it can be seen that the pinning potentials are higher in the (15Pr/843nmY)x3 and (15Pr/885nmY)x6 quasi-multilayers.

The most accurate measurements of the critical current density, which do not imply any theoretical model like in the case of magnetic measurements, are the ***transport measurements***, which is a 4-contact measurement. For this method, a narrow bridge needs to be etched, as described in Chapter 2, and contacts need to be prepared and connected to a current source and a digital voltmeter. In our case, the transport measurements are integrated in the Quantum Design PPMS with the transport with rotator option set, which allowed us to determine J_c at different angles θ between the film surface and applied magnetic fields. Critical current density is automatically determined by the PPMS software from the current-voltage characteristics, using ussualy a voltage criterion of 1 μV/cm. For example, the angle dependence of J_c in an applied field of 1 T, at various temperatures from 77.3 K to 83 K, for a substrate-decorated film (15Ag/450nmYBCO)x1 is shown in Figure 20. In these rotating scans, angles $\theta = 0^o$, 180^o and 360^o correspond to the direction of magnetic field along the c-axis of the sample while the angles at $\theta = 90^o$ and 270^o corresponding to the direction of magnetic field along the ab-plane of the sample (film surface). It can be seen that the values of J_c along the ab-plane are maximum at all temperatures for this field. The temperature dependence of J_c in 1 T, along the c-axis and in the ab-plane, is shown in Figure 21 (left-hand side), while the temperature dependence of their ratio, J_c^{ab}/J_c^{c}, is shown in the right-hand side of the figure. It can be seen that at temperatures higher than 84 K, this ratio is close to 1. J_c of a (15Ag/450nmYBCO)x10 quasi-multilayer film as a function of θ, in several fields at a temperature of 82 K, is plotted in Figure 22. Overall, the curves in the figure look quite similar to those of the YBCO grown on Ag-decorated substrate shown in Figure 20, but a closer look at the curves in high fields from 3 to 6 T show some small additional peaks along the c-axis at 0^o and 180^o, which were not observed for single layer film in 1 T, which indicates that angular dependence of J_c of multilayer films can give additional information on the nature of pinning centres. In higher field of 6T, the secondary peak along the c-axis appears at all temperatures from 77.3 K to 82 K, as shown in Figure 23. This secondary peak is attributed to c-axis correlated extended defects created by Ag nanodots. The isotropic or anisotropic nature of pinning centres created by Ag quasi-layers can be clarified by scaling the angle dependence of critical current density $J_c(\theta,H)$. One of the approaches uses direct Blatter's et al. scaling [61] based on the anisotropic Ginzburg-Landau theory. In this approach, which was first proposed by Civale et al. [62], the isotropic and anisotropic pinning centres can be identified from a plot of J_c versus effective magnetic field $H_{eff} = \varepsilon(\theta)H$, where $\varepsilon^2(\theta) = \cos^2\theta + \gamma^{-2}\sin^2\theta$, γ is the anisotropy factor, (γ = 5-7 for YBCO single crystal), and θ is

the angle between the magnetic field and *c*-axis of YBCO. However, later was shown that, in YBCO films with artificial pinning centres, the parameter γ in the scaling is not the effective mass anisotropy, having values usually much less than for single crystals [63]. The plot of $J_c(\theta)$ and the rescaled plot $J_c(H_{eff})$ of (15Ag/450nmYBCO)x10 multilayer film at 77.3 K and in 6 T are shown in Figure 24. The points A and B help to visualise how the various angular regions are transformed by the rescaling. In Figure 24a the full line represent the one-parameter fit with Blatter's formula for the parameter $\gamma = 3$. The plot is repeated for every field for several parameters γ and the rescaled curves are plotted in the same graph, until the right parameter γ is found in which all data collapse onto a single smooth decreasing curve, except for those points corresponding to the angular regions close to *H*//*ab* (point *B*) and *H*//*c* (point *A*) for each field, as shown in Figure 25. We find that by using the effective mass anisotropy γ=7, the curves do not collapse (Figure 25a), while for γ = 3 (Figure 25b) the best collapse of the curves is achieved. This value is smaller than that in pure YBCO film, but larger than in the case of films with strong pinning centres grown chemically [63]. The peak at *H*//*ab* represent the intrinsic pinning contribution (Tachiki-Takahashi), which arises mainly from the modulation of the superconducting order parameter along the *c* direction, as a consequence of the layered crystallographic structure and of course, it can also include the contribution of other correlated structures parallel to the *ab* planes. The weaker peak at *H*//*c* is due to correlated disorder along the *c* axis, such as twin boundaries, linear and columnar defects. In the case of films grown from BZO-doped YBCO target, transport measurements revealed huge differences in angle dependence of J_c between films grown at 780 ^oC and 8 Hz, and, at higher temperature and lower frequency (800 ^oC and 3 Hz, as can be seen in Figure 26. Qualitatively, one can clearly see the difference in the peak along the *ab*-planes and the peak along the *c*-axis of the two films, with the film deposited at lower temperature and higher frequency showing larger J_c with the field along the *ab*-plane, but with a ratio between J_c^c/J_c^{ab} close to unity (0.91), while the film deposited at higher temperature and lower frequency has larger J_c for field along the *c*-axis, with J_c^c/J_c^{ab}=1.84. These results are a confirmation of the fact that larger deposition temperatures and lower frequency of laser pulses promote the self-assembling of BZO nano-particles into *c*-axis oriented and splayed columnar structures that are effective pinning centres for flux lines oriented close to *c*-axis [55]. However, the angle dependence of J_c is not trivial, and depends on the values of the applied field, as can be seen in Figure 27. For fields up to 2 T, J_c^c is larger than J_c^{ab} (with quite a smooth dependence at 2 T), while from 2.5 T the sample returns to the "usual"

situation in which J_c^c is smaller than J_c^{ab}, meaning that the density of *c*-axis correlated defects is not large enough to pin all the flux lines at high fields. By using the BZO-doped target in combination with Ag nano-dots in both substrate decoration or quasi-multilayer approaches, the critical current density for fields parallel to the c-axis is increased (even with a local maximum in high fields), as can be seen in Figure 28. Apart from J_c^c increasing, J_c^{ab} is also larger. Of course, in these conditions the collapsing of all curves using the rescaling approach does not work. Instead, the angle dependence of critical current in films with such complex pinning landscape can be fitted with a model proposed by Long [64] which describes the statistical process of the pinning of many vortex segments on *c*-axis extended defects and planar *ab*-plane pinning sites (random walk), with an addition that takes into account trapping of flux during the record of $I_c(\theta)$. Such a description can explain even small details of $I_c(\theta)$, as can be seen in Figure 29.

Transmission electron microscopy studies revealed various types of defects, both "natural" and nano-engineered: nanoparticles of Cu-rich phases, nanoparticles of Y_2O_3, grain boundaries, misfit dislocations, BZO nanoparticles, BZO nano-rods oriented mainly in the *c*-axis direction, but some are splayed extended defects. Few examples are shown in Fig. 30. The best results in terms of current density and its anisotropy has been obtained in films with integrated nanotechnology of pinning centres that created synergetic pinning centres. TEM image shown in Fig. 31 for a Ag/BZO-doped YBCO quasi-multilayer is fundamentally different from BZO nanorods in samples reported elsewhere [18, 33, 37, 55]. While the other samples demonstrate BZO nanorods embedded in the matrix of YBCO, this sample is structurally close to a dense entanglement of long BZO and YBCO nanothreads. The threads are extended for more than 1.5 μm and through the whole thickness of the sample. We suggest that the formation of such a structure is due to the specific property of Ag nanoparticles to dissolve YBCO and provide its local epitaxial growth while moving out of them film–substrate interface. The YBCO threads are visible as long white features of a width of about 10–20 nm (few of them outlined as guide to the eye). The BZO nanothreads are in the dark areas. Not all dark Moiré fringes belong to BZO nanorods as BZO content in the sample is only 4%. Some fringes belong to the boundaries between YBCO nanothreads. A lower part of BZO nanothread marked 1 in the plot is hidden behind the YBCO.

IV. Conclusions

A range of methods with different type of nanoparticles self-assembly has been explored in order to increase critical current in YBCO superconducting films in magnetic fields. The use of Ag nano-dots in the quasi-multilayer approach allows growth of thick films (up to 5-6 μm) with improved properties and a columnar growth of the YBCO. It is found that that type of self-assembly plays an important role and that combination of two-dimensional self-assembly on the surface of substrate with formation of nanorods of the external phase provides highest critical current comparing to other already known methods. In quite large range of applied fields, the critical current anisotropy is very low, which is very important for solenoid applications. Pinning potential estimated from frequency dependent ac susceptibility measurements are consistent with Zeldov's logarithmic dependence on current density. Analysis of bulk pinning forces in the frame-work of Dew-Hughes showed that two-dimensional normal pinning is prominent, in good agreement with TEM images.

Acknowledgements

This work has been supported by the Marie Curie Excellence Grant MEXT-CT-2006-041111 "NanoTechPinning HTS"; by the COST Action MP 1201 "Nanoscale SuperConductivity:Novel Functionalities through Optimized Confinement of Condensate and Fields "; and by Romanian Ministry of national Education and Research through Core Programme PN16-480102 "Synthesis and characterisation of nanostructured materials, thin films and hetherostructures" and POC-A.1-A.1.1.4-E2015 Project P_37_697 "Boron- and rare-earths-based advanced functional materials". V.S.D would also like to acknowledge the support for equipment of Nano and Energy Center, VNU-Hanoi University of Science, Vietnam.

References

[1] R.M. Hazen, L.W. Finger, R.J. Angel, C.T. Prewitt, N.L. Ross, H.K. Mao, C.G. Hadidiacos, P.H. Hor, R.L. Meng, C.W. Chu, Physical Review B 35 (1987) 7238.

[2] S.R. Foltyn, L. Civale, J.L. Macmanus-Driscoll, Q.X. Jia, B. Maiorov, H. Wang, M. Maley, Nature Materials 6 (2007) 631.

[3] J.M. Huijbregtse, F.C. Klaassen, A. Szepielow, J.H. Rector, B. Dam, R. Griessen, B.J. Kooi, J.T.M. de Hosson, Superconductor Science & Technology 15 (2002) 395.

[4] L. Civale, A. D. Marwick, T. K.Worthington, M. A. Kirk, J. R. Thompson, L. Krusin-Elbaum, Y. Sun, J. R. Clem, and F. Holtzberg, Physical Review Letter 67 (1991) 648.

[5] L. Civale, Superconductor Science & Technology 10 (1997) A11.

[6] H. Kito, A. Iyo, M. Hirai, A. Crisan, M. Tokumoto, S. Okayasu, M. Sasase and H. Ihara, Physica C 378 (2002) 329.

[7] A. Crisan, S.K. Agarwal, T. Koganezawa, R. Kuroda, K. Tokiwa, T. Watanabe, A. Iyo, Y. Tanaka, H. Ihara, Journal of Physics and Chemistry Solids 63 (2002) 1073.

[8] V. Mihalache, G. Aldica, S. Popa, P. Nita, and A. Crisan, Journal of Superconductivity 14 (2001) 381.

[9] A.V. Berenov, R. Marriott, S.R. Foltyn, J.L. MacManus-Driscoll, IEEE Transactions on Applied Superconductivity 11 (2001) 3780.

[10] V. Mihalache, G. Aldica, S. Popa, and A. Crisan, Physica C 384 (2003) 451.

[11] P. Badica, A. Iyo, G. Aldica, H. Kito, A. Crisan, and Y. Tanaka, Superconductor Science & Technology 17 (2004) 430.

[12] L.Miu, A. Crisan, S. Popa, V. Sandu, L. Nistor, Journal of Superconductivity 3 (1990) 391.

[13] L. Miu, S. Popa, A. Crisan, G. Aldica, J. Jaklovszky, Journal of Superconductivity 6 (1993) 279.

[14] M. Baert, V. V. Metlushko, R. Jonkheere, V. V. Moshchalkov, and Y. Bruynseraede, Physical Review Letter 74 (1995) 3269.

[15] A. Crisan, A. Pross, D. Cole, S.J. Bending, R. Wördenweber, P. Lahl, E.H. Brandt, Physical Review B 71 (2005) 144504.

[16] A. Crisan, S. Fujiwara, J.C. Nie, A. Sundaresan, H. Ihara, Applied Physics Letters 79 (2001) 4547.

[17] T. Haugan, P.N. Barnes, R. Wheeler, F. Meisenkothen, M. Sumption, Nature 430 (2004) 867.

[18] J.L. MacManus-Driscoll, S.R. Foltyn, Q.X. Jia, H. Wang, A. Serquis, L. Civale, B. Maiorov, M.E. Hawley, M.P. Maley, D.E. Peterson, Nature Materials 3 (2004) 439.

[19] A. Crisan, P. Badica, S. Fujiwara, J.C. Nie, A. Sundaresan, Y. Tanaka and H. Ihara, Applied Physics Letter 80 (2002) 3566.

[20] A. Crisan, P. Badica, S. Fujiwara, J.C. Nie, A. Sundaresan, A. Iyo, and Y. Tanaka, , IEEE Transactions on Applied Superconductivity 13 (2003) 3726.

[21] M. Ionescu, A.H. Li, Y. Zhao, H.K. Liu and A. Crisan, Journal of Physics D: Applied Physics 37 (2004) 1824

[22] P. Badica, A. Sundaresan, A. Crisan, J.C. Nie, M. Hirai, S. Fujiwara, H. Kito and H. Ihara, Physica C 383 (2003) 482.

[23] K. Matsumoto, T. Horide, K. Osamura, M. Mukaida, Y. Yoshida, A. Ichinose, and S. Horii, Physica C 412-414 (2004) 1267.

[24] P. Mele, K. Matsumoto, T. Horide, O. Miura, A. Ichinose, M. Mukaida, Y. Yoshida, and S. Horii, Superconductor Science & Technology 19 (2006) 44.

[25] J.C. Nie, H. Yamasaki, H. Yamada, Y. Nakagawa, K. Develos-Bagarinao, and Y. Mawatari, Superconductor Science & Technology 17 (2004) 845.

[26] T. Aytug, M. Paranthaman, A.A. Gapud, S. Kang, H.M. Christen, K.J. Leonard, P.M. Martin, J.R. Thompson, D.K. Christen, R. Meng, I. Rusakova, C.W. Chu, and T.H. Johansen, Journal of Applied Physics 98 (2005) 114309.

[27] P. Mikheenko, A. Sarkar, V.S. Dang, J.L. Tanner, M.M. Awang Kechik, J.S. Abell, and A. Crisan, IEEE Transactions on Applied Superconductivity 19 (2009) 3491.

[28] P.N. Barnes, T.J. Haugan , C.V. Varanasi, T.A. Campbell, Applied Physics Letters 85 (2004) 4088.

[29] C. Cai, J. Hänisch, R. Hühne, V. Stehr, C. Mickel, T. Gemming, and B. Holzapfel, Journal of Applied Physics 98 (2005) 123906.

[30] C. Cai, J. C. Zhang, S.X. Cao, J. Hänisch, R. Hühne, and B. Holzapfel, Physica C 460-462, (2007) 1355.

[31] E. Backen, J. Hänisch, R. Hühne, K. Tscharntke, S. Engel, T. Thersleff, L. Schultz, and B. Holzapfel, IEEE Transactions on Applied Superconductivity 17 (2007) 3733.

[32] J. Hänisch, C. Cai, V. Stehr, R. Hühne, J. Lyubina, K. Nenkov, G. Fuchs, L. Schultz, and B. Holzapfel, Superconductor Science & Technology 19 (2006) 534.

[33] A. Goyal, S. Kang, K. J. Leonard, P.M. Martin, A.A. Gapud, M. Varela, M. Paranthaman, A.O. Ijaduola, E.D. Specht, J.R. Thompson, D.K. Christen, S.J. Pennycook, and F.A. List, Superconductor Science & Technology 18 (2005) 1533.

[34] A. Crisan, M.M. Awang Kechik, P. Mikheenko, A. Sarkar, J.S. Abell, P. Paturi, H. Huhtinen, Superconductor Science & Technology. 22 (2009) 045014.

[35] S. Horii, K. Yamada, H. Kai, A. Ichinose, M. Mukaida, R. Teranishi, R. Kita, K. Matsumoto, Y. Yoshida, J. Shimoyama, K. Kishio, Superconductor Science & Technology 20 (2007) 1115.

[36] K. Yamada, A. Ichinose, S. Yasunaga, R. Teranishi, M. Mukaida, S. Horii, R. Kita, S. Kato, Y. Yoshida, K. Matsumoto, S. Toh, Japanese Journal of Applied Physics 47 (2008) 899.

[37] P. Mele, K. Matsumoto, T. Horide, A. Ichinose, M. Mukaida, Y. Yoshida, S. Horii, R. Kita, Superconductor Science & Technology 21 (2008) 032002.

[38] M.M. Awang Kechik, P. Mikheenko, A. Sarkar, V.S. Dang, N. Hari Babu, D.A. Cardwell, J.S. Abell and A. Crisan, Superconductor Science & Technology 22 (2009) 034020.

[39] A. Koblischka-Veneva, F. Mucklich, M.R. Koblischka, N.H. Babu, D.A. Cardwell, Journal of the American Ceramic Society 90/8 (2007) 2582

[40] S.A. Harrington, J.H. Durrell, B. Maiorov, H. Wang, S.C. Wimbush, A. Kursumovic, J.H. Lee, J.L. MacManus-Driscoll, Superconductor Science & Technology 22, (2009) 022001.

[41] G. Ercolano, S.A. Harrington, H. Wang, C.F. Tsai, J.L. MacManus-Driscoll, Superconductor Science & Technology 23, (2010) 022003.

[42] S.H, Wee, A. Goyal, E.D. Specht, C. Cantoni, Y.L. Zuev, V. Selvamanickam, S. Cook, Physical Review B 81 (2010) 140503.

[43] H.H. Wen, R.L. Wang, H.C. Li, B. Yin, S.Q. Guo, Z.X. Zhao, S.L. Yan, L. Fang, and M.S. Si, Physical Review B 54 (1996) 1386.

[44] A.H. Li, H.K. Liu, M. Ionescu, X.L. Wang, S.X. Dou, E.W. Collings, M.D. Sumption, M. Bhatia, Z.W. Lin and J.G. Zhu, Journal of Applied Physics 97 (2005) 10B107.

[45] D. Dew-Hughes, Philosophical Magazine 30 (1974) 293.

[46] E.H. Brandt, Physical Review B 49 (1994) 9024.

[47] M. Tinkham, *Introduction to Superconductivity* 2nd ed. (McGraw-Hill, New York), p. 355 (1996).

[48] P.W. Anderson and Y.B. Kim, Reviews of Modern Physics 36 (1964) 39.

[49] A. Crisan, Journal of Superconductivity 7 (1994) 687.

[50] G. Blatter, M.V. Feigel'man, V.B. Geshkenbein, A.I. Larkin, V.M. Vinokur, Reviews of Modern Physics 66 (1994) 1125.

[51] E. Zeldov, N.M. Amer, G. Koren, A. Gupta, R.J. Gambino, M.W. McElfresh, Physical Review Letters 62 (1989) 3093.

[52] E. Zeldov, N.M. Amer, G. Koren, A. Gupta, M.W. McElfresh, R.J. Gambino, Applied Physics Letters 56 (1990) 680.

[53] P. Mikheenko, A. Sarkar, V.-S. Dang, J. L. Tanner, J. S. Abell, and A. Crisan, Physica C: Superconductivity and its Applications, 469 (2009) 798.

[54] P. Mikheenko, J.L. Tanner, J. Bowen, A. Sarkar, V.-S. Dang, J.S. Abell, A. Crisan, Physica C: Superconductivity and its Applications, 470 (2010) S234.

[55] B. Maiorov, S. A. Baily, H. Zhou, O. Ugurlu, J. A. Kennison, P. C.Dowden, T. G. Holesinger, S. R. Foltyn, and L. Civale, Nature Materials, 8 (2009) 398.

[56] M. Peurla, H. Huhtinen, P. Paturi, Superconductor Science & Technology, 18 (2005) 628.

[57] P. Mikheenko, V.-S. Dang, Y.Y. Tse, M. M. Awang Kechik, P. Paturi, H. Huhtinen, Y. Wang, J. S. Abell and A. Crisan, Superconductor Science & Technology, 23 (2010) 125007.

[58] P. Mikheenko, V.-S. Dang, M. M. Awang Kechik, A. Sarkar, P. Paturi, H. Huhtinen, J. S. Abell and A. Crisan, IEEE Transactions on Applied Superconductivity 21(3) (2011) 3184.

[59] B. Dam, J.M. Huijbregtse, F.C. Klaassen, R.C.F. van der Geest, G. Doornbos, J.H. Rector, A.M. Testa, S. Freisem, J.C. Martinez, B. Stäuble-Pümpin and R. Griessen, Nature 399 (1999) 439.

[60] B. Dam, J.M. Huijbregtse, R.C.F. van der Geest, F.C. Klaassen, J.H. Rector, I.L. Elberse, and R. Griessen, Physica C 341-348 (2000) 2327.

[61] G. Blatter, V.B. Geshkenbein, A.I. Larkin, Physical Review Letters 68 (1992) 875.

[62] L. Civale, B. Maiorov, A. Serquis, J.O. Willis, J.Y. Coulter, H. Wang, Q.X. Jia, P.N. Arendt, M. Jaime, J.L. MacManus-Driscoll, M.P. Maley, S.R. Foltyn, Journal of Low Temperature Physics 135 (2004) 87.

[63] J. Gutierrez, A. Llordes, J. Gazquez, M. Gibert, N. Roma, S. Ricart, A. Pomar, F. Sandiumenge, N. Mestres, T. Puig, X. Obradors, Nature Materials 6 (2007) 367.

[64] N. J. Long, Superconductor Science & Technology 21 (2008) 025007.

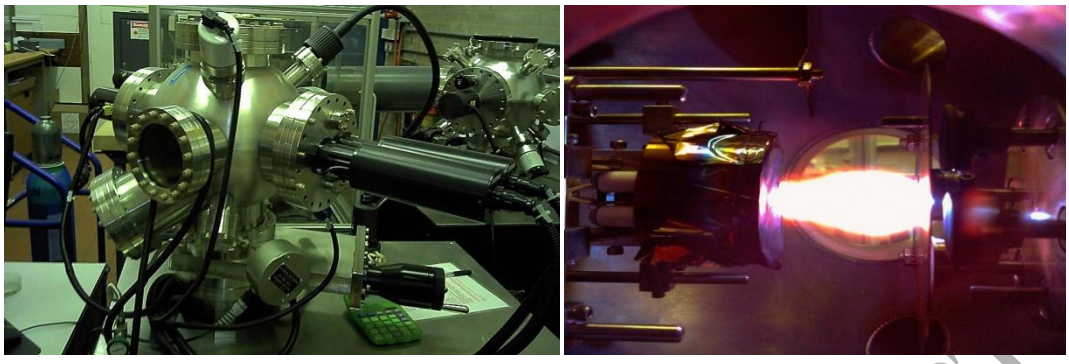

Fig. 1. PLD chamber (left-hand side) and laser plume image inside the chamber during deposition (right-hand side)

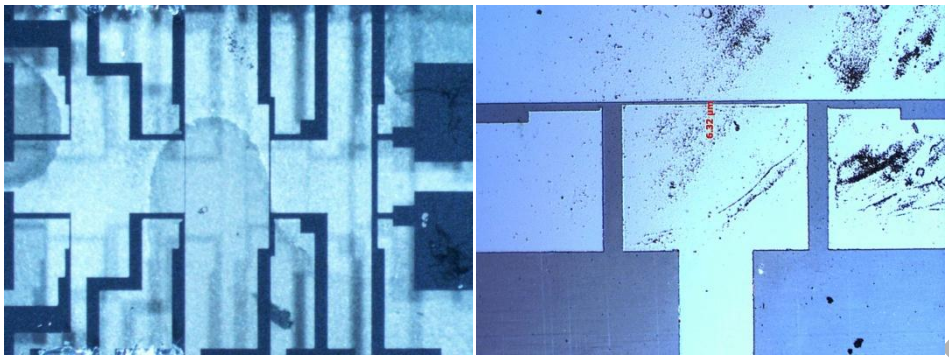

Fig. 2. YBCO film with 4 bridges etched, having widths between 6 and 50 μm (left-hand side), and image of the smallest (6.3 μm width) surviving bridge (right-hand side)

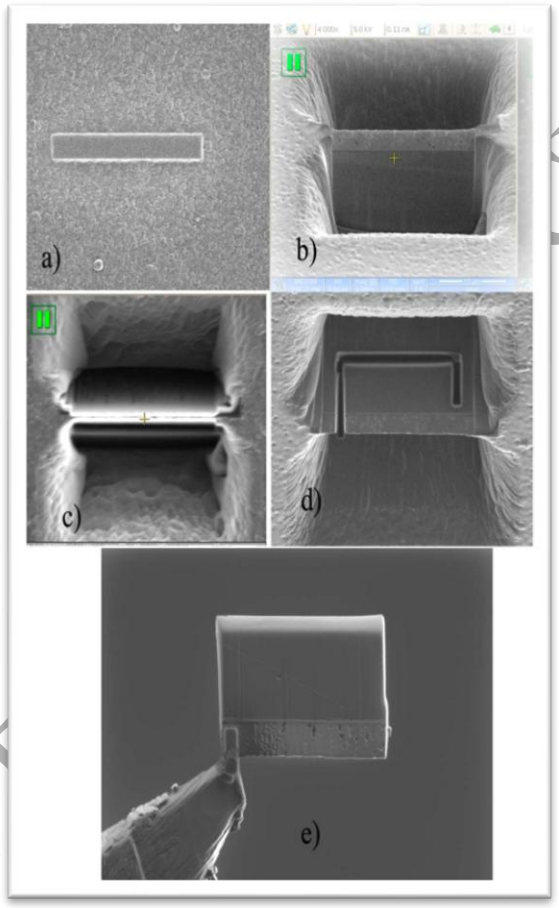

Fig. 3. FIB process of preparing specimens for Transmission Electron Microscopy; a) cover sample, b) mill sample, c) cleaning, d) cut, e) stick on a grid and then thinning

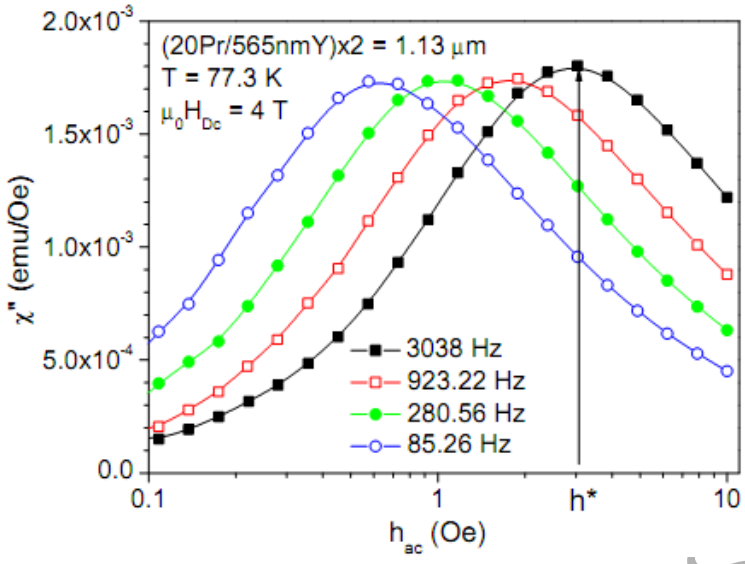

Fig. 4. Example of AC field dependence of χ" at various frequencies, at 77.3 K and in 4 T, of a PBCO/YBCO quasi-multilayer (2 quasi-layers of $PrBa_2Cu_3O_7$ nano-dots interspaced with 2 565 nm-thick YBCO layers).

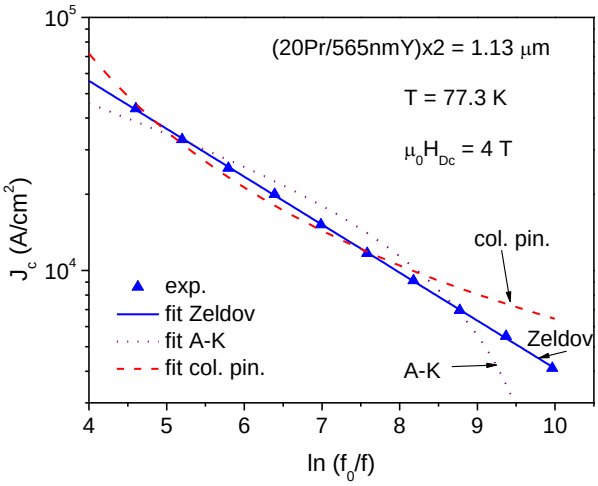

Fig. 5. Frequency dependence of critical current density for the same sample and temperature and field conditions as in Fig. 4. Dotted, dashed and full lines represent fits with Anderson-Kim, collective pinning, and Zeldov model, respectively (see text).

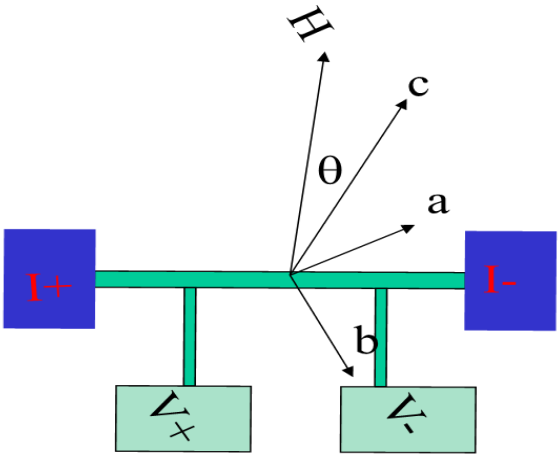

Fig. 6. Scheme of AC transport with rotation measurement of an YBCO bridge.

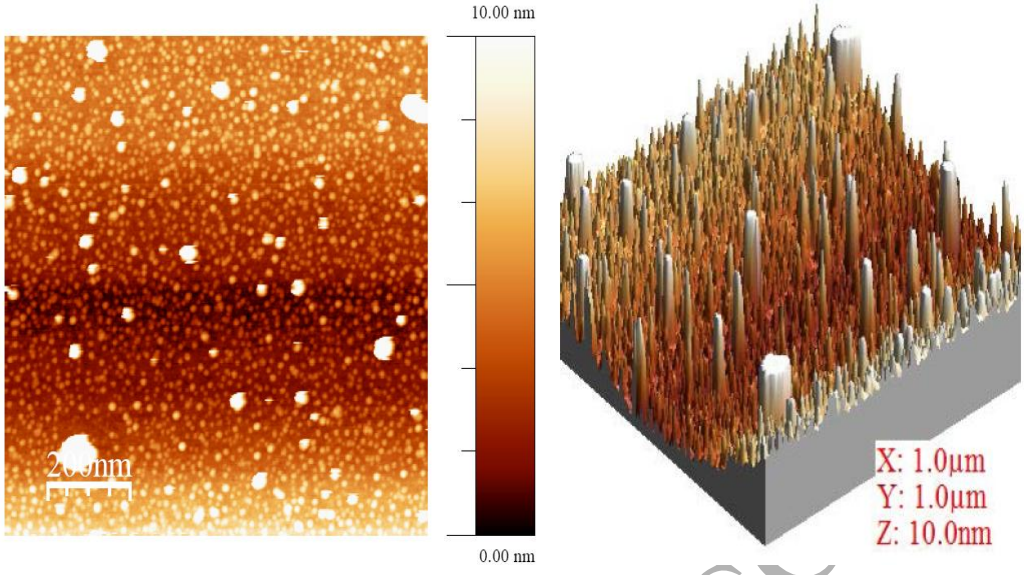

Fig. 7. AFM image of the distribution of Ag nano-dots grown at 400 ^{o}C with 25 laser pulses on silver target.

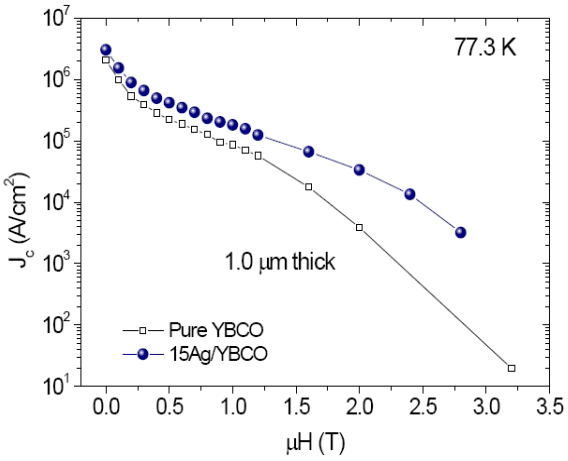

Fig. 8. Field dependence of critical current densities of 1μm-thick YBCO films grown on STO and on STO decorated with 15 laser pulses on Ag target at 400 400 ^{o}C.

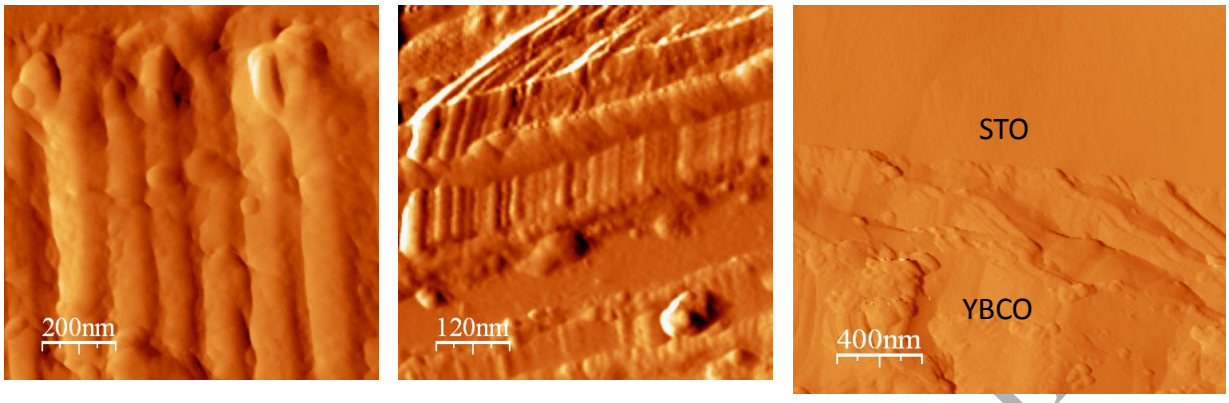

Fig. 9. AFM (side view) of YBCO grown on (from left to right): Au nano-dots decorated substrate, Ag nano-dots decorated substrate and on bare substrate.

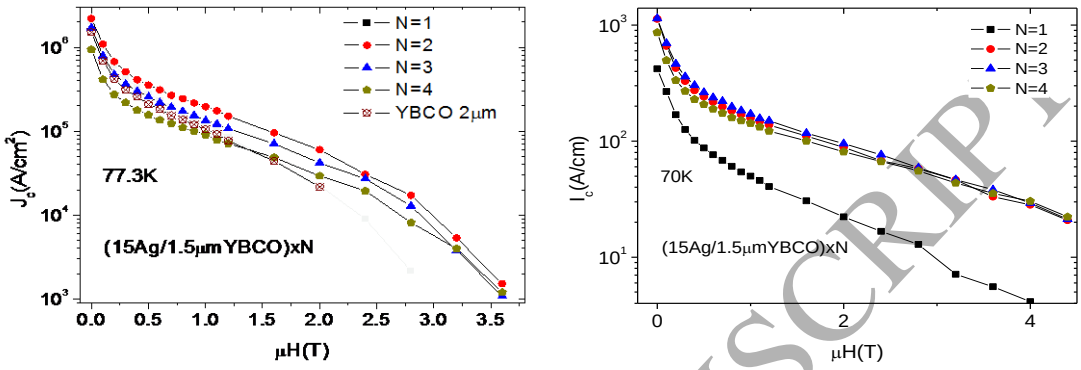

Fig. 10. Field dependence of J_c of (15Ag/1.5μmYBCO)xN multilayer films at 77.3 K (left-hand side) and of the the critical current I_c at 70 K).

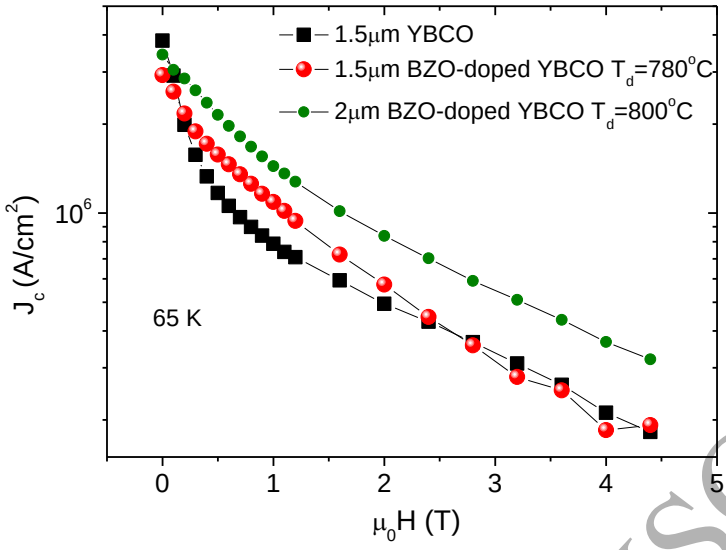

Fig. 11. Field dependence of J_c at 65 K of BZO-doped YBCO film deposited at 780^{o}C and 8 Hz and at 800^o C and 3 Hz in comparison with J_c of YBCO film grown at 780^o C and 8 Hz.

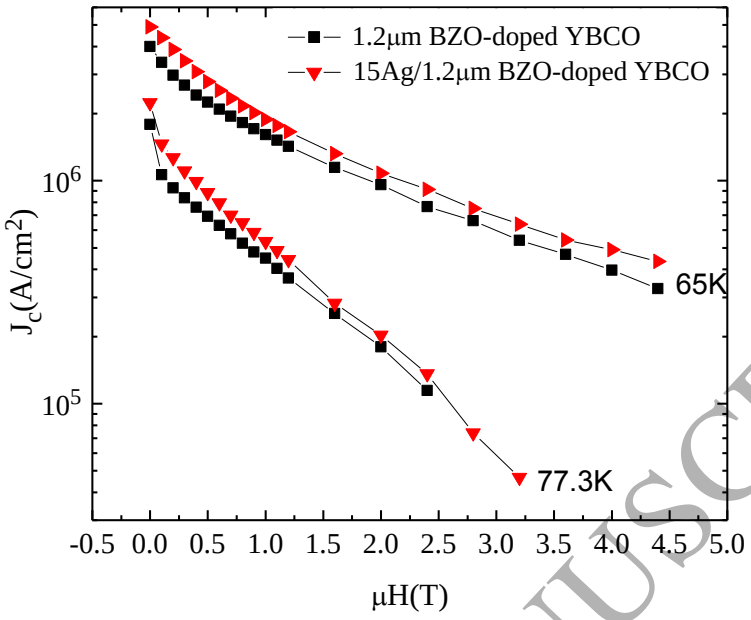

Fig. 12. Magnetic field dependence of J_c at 65K and 77.3 K of BZO-doped YBCO film grown on Ag decorated substrate (red triangles) and of BZO-doped YBCO film grown on bare substrate (black squares) with the same thickness of 1.2 μm.

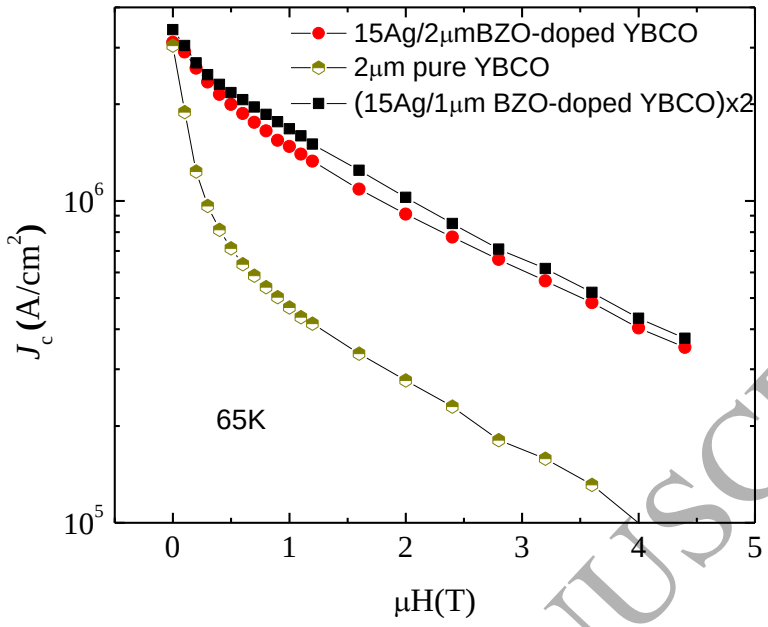

Fig. 13. Field dependence of J_c at 65 K of a single Ag/BZO-doped YBCO layer and a double Ag/BZO-doped YBCO layer, in comparison with pure YBCO film, all having the same thickness.

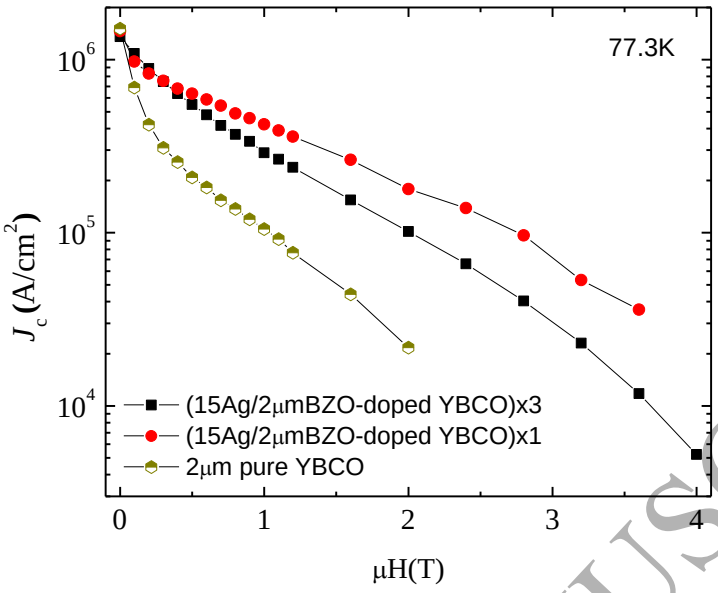

Fig. 14. Field dependence of J_c of a 2μm-thick Ag/BZO-doped YBCO single layer, a 6μm-thick Ag/BZO-doped YBCO trilayer and a 2.0 μm-thick pure YBCO single layer at 77.3 K.

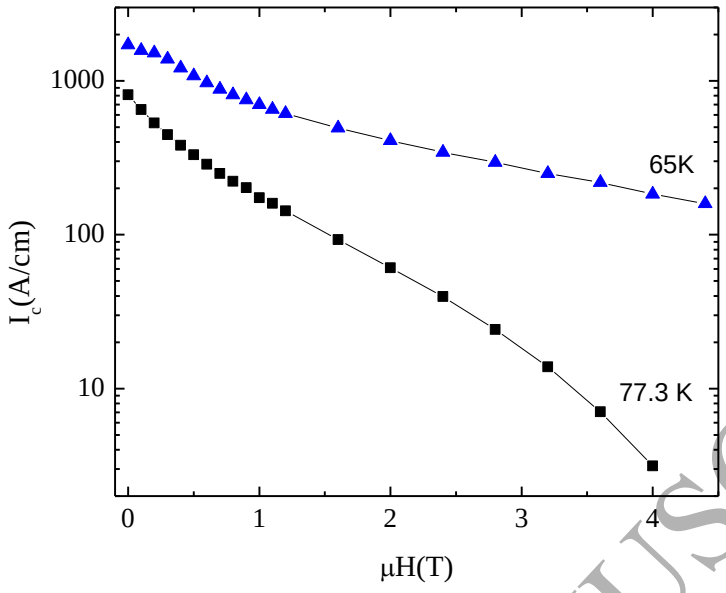

Fig. 15. Critical current per cm width of 6 μm Ag/BZO-doped YBCO tri-layer film at 65 K and 77.3 K.

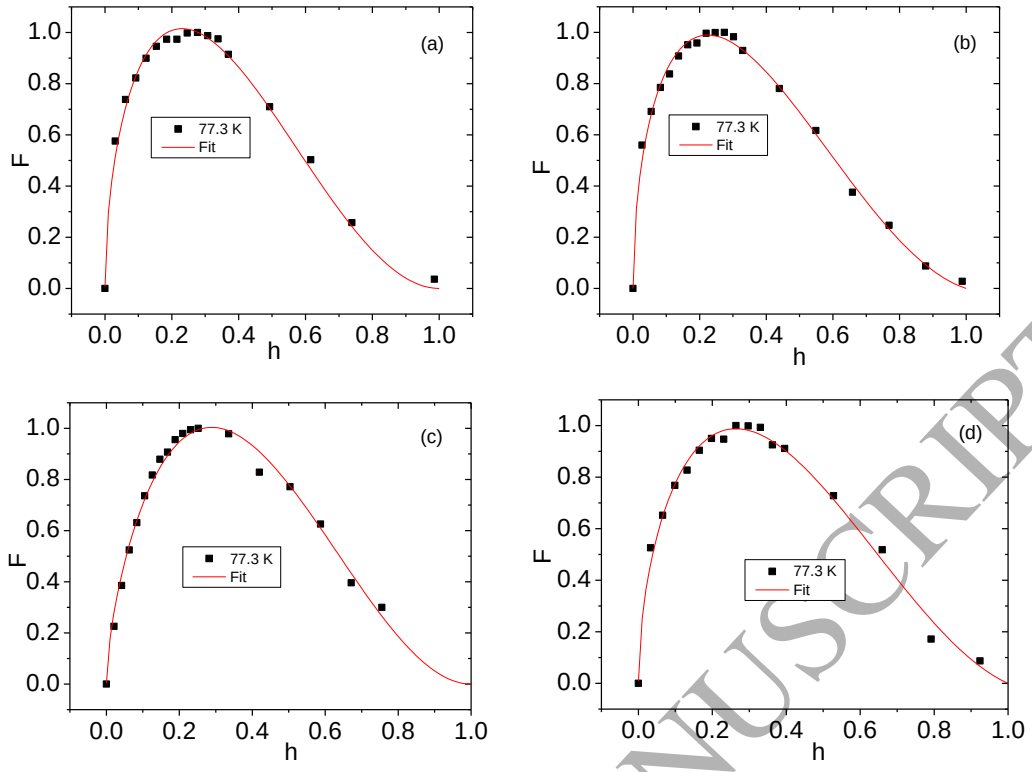

Fig. 16. Plots of the experimental data with fitting functions for (a) 2 μm of YBCO deposited at 780˚C, (b) (15Ag/1.5μmYBCO)x2, (c) 15Ag/2.0μm BZO-doped YBCO, and (d) (15 PBCO/0.5 μm YBCO)x3 quasi-multilayer.

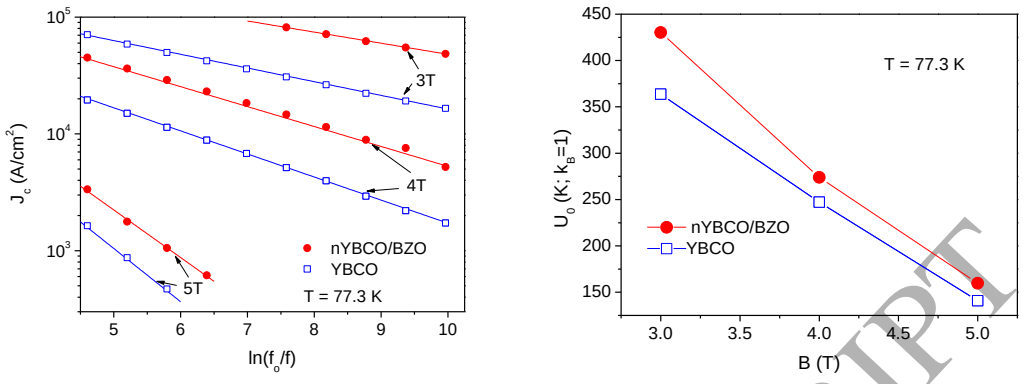

Fig. 17. Frequency dependence of J_c (left-hand side) and DC field dependence of pinning potential (right-hand side) of two 1.27 μm – thick films, ablated from a nano-crystalline $YBa_2Cu_3O_{7-\delta}$ (YBCO) target doped with 4 wt.% $BaZrO_3$ (BZO), nYBCO/BZO, and from a commercial micro-crystalline pure YBCO target.

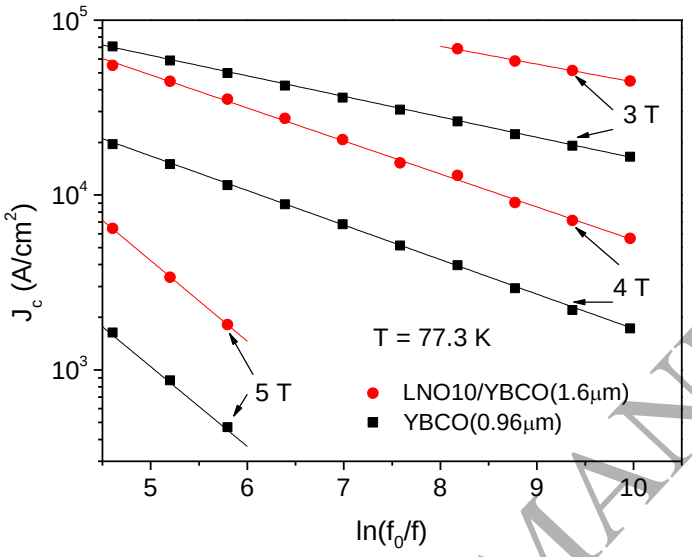

Fig. 18. Frequency dependence of J_c for a 1.6 μm – thick film grown on STO substrate decorated with $LaNiO_3$ nano-dots grown by 10 laser pulses at 200 °C and 10 mTorr oxygen pressure, in comparison with a 0.96 μm – thick film grown on bare substrate, in DC magnetic fields of 3, 4 and 5 T. Full lines are linear fits in a double-logarithmic scale.

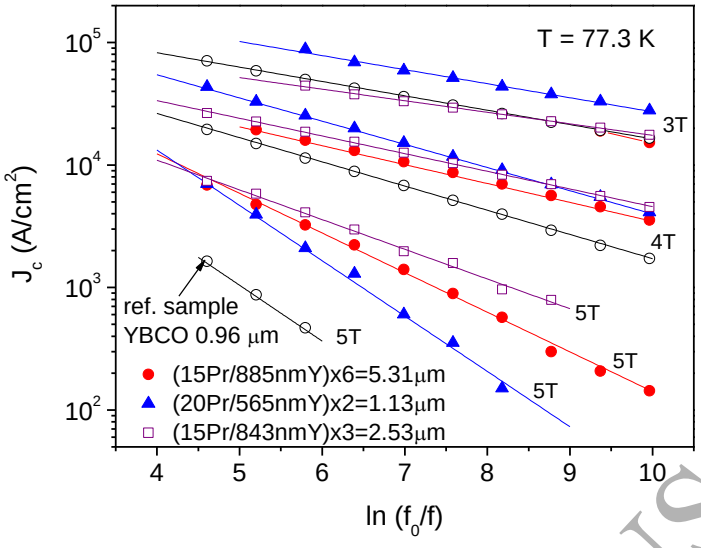

Fig. 19. Frequency dependence of J_c for the PrBCO/YBCO quasi-multilayers, and, for comparison, of the 0.96 μm – thick film grown on bare substrate, in DC magnetic fields of 3, 4 and 5 T, at 77.3 K.

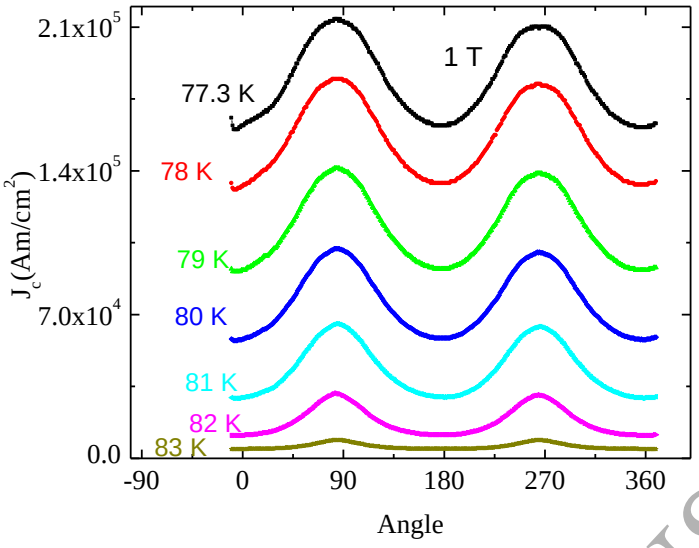

Fig. 20. Angle-dependent critical current density of (15Ag/ 450 nmYBCO)x1 in 1 T and at different temperatures from 77.3 to 83 K

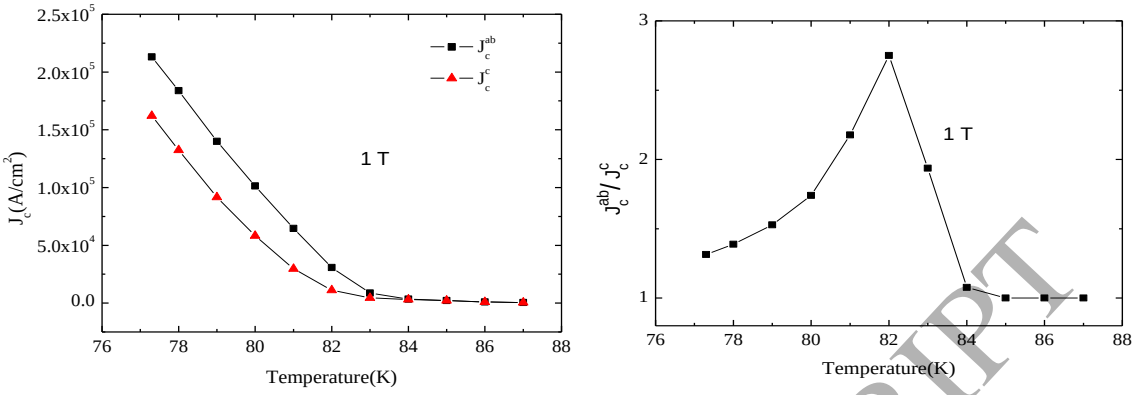

Figure 21. Temperature dependence of J_c^{ab} and J_c^{c} (left-hand side) and temperature dependence of the ratio J_c^{ab}/J_c^{c} (right hand side) in 1 T for the same sample as in Figure 20.

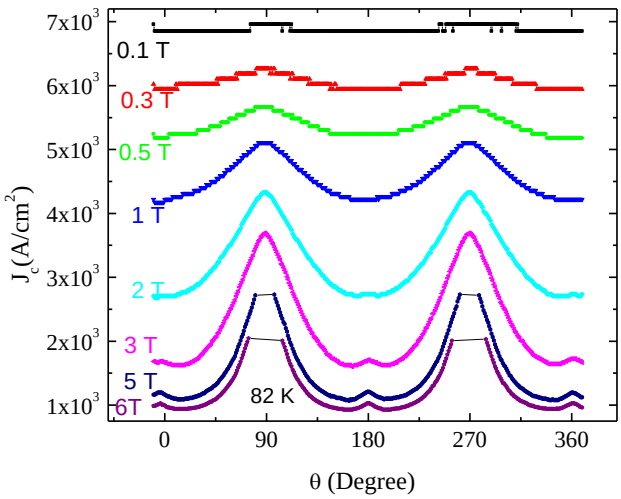

Fig. 22. Angular dependence of J_c at several fields, indicated on the left hand side of each curve, at T = 82 K for a (15Ag/450 nm YBCO) x 10 quasi-multilayer film.

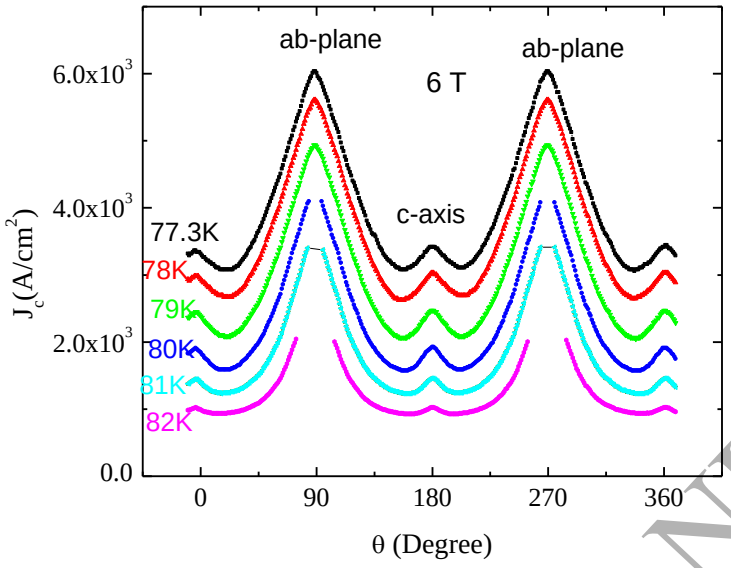

Fig. 23. Angular dependence of J_c at several temperatures in 6 T for (15Ag/450nmYBCO)x10 quasi-multilayer film.

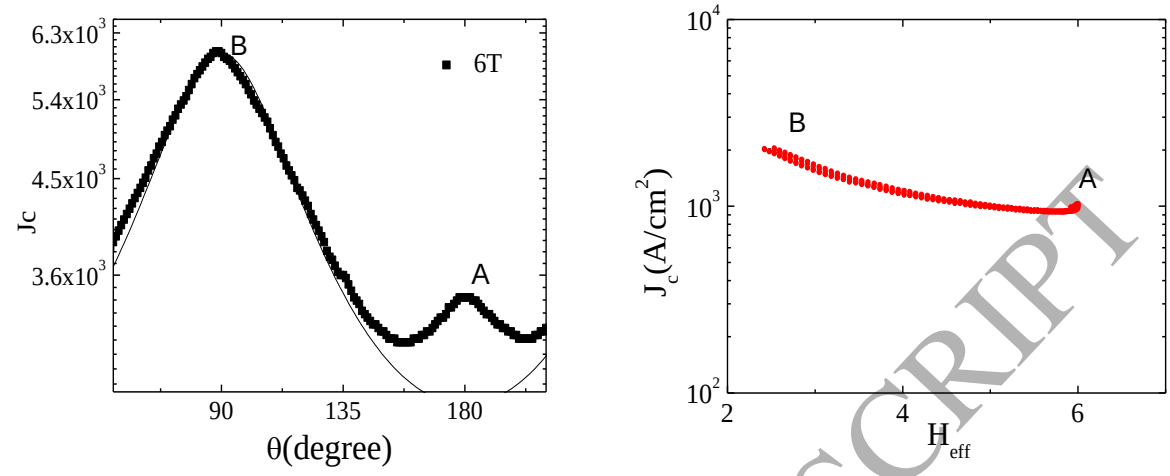

Fig. 24. Angular dependence of J_c of (15Ag/450nmYBCO)x10 multilayer film at 77.3 K and in 6 T, A and B indicate the peaks for $H//c$ and ab, respectively (a); and J_c as a function of H_{eff} for the same data, with $\gamma = 3$ used to calculate H_{eff}

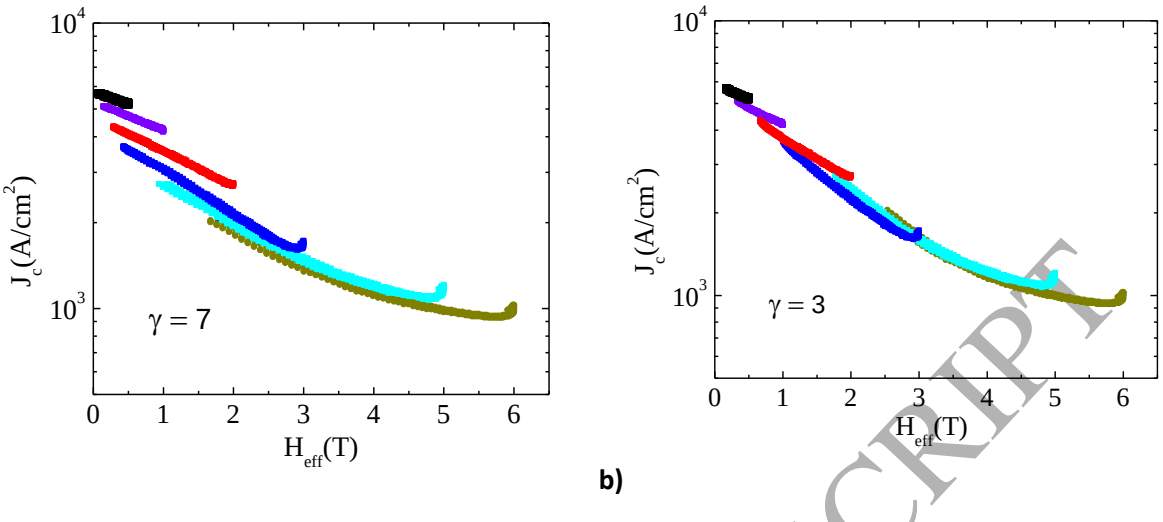

Fig. 25. J_c as a function of H_{eff} for all applied fields; with H_{eff} calculated using $\gamma = 7$ (effective mass anisotropy of YBCO) the data $J_c(H_{eff})$ do not collapse in a single curve (a), with H_{eff} calculated using $\gamma = 3$, the data of $J_c(H_{eff})$ collapsed quite well in a single curve (b).

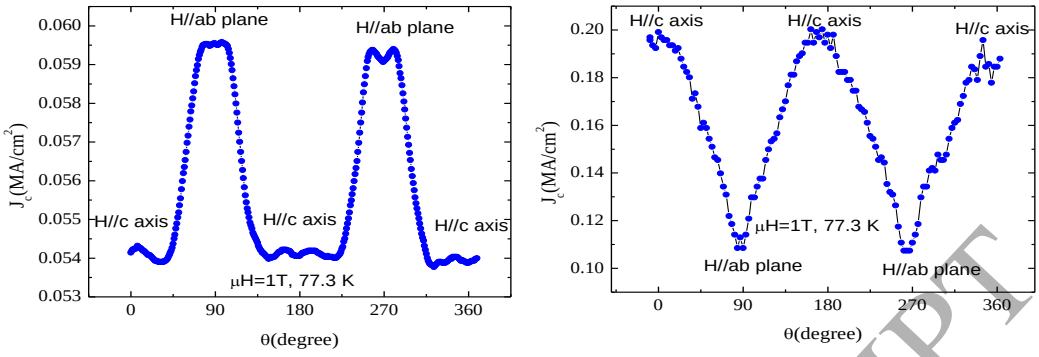

Fig. 26. Angle dependence of critical current density at 77.3 K and 1 T, for BZO-doped YBCO films grown at 780^{o} C and 8 Hz (left-hand side) and, respectively 800^{o} C and 3 Hz (right-hand side).

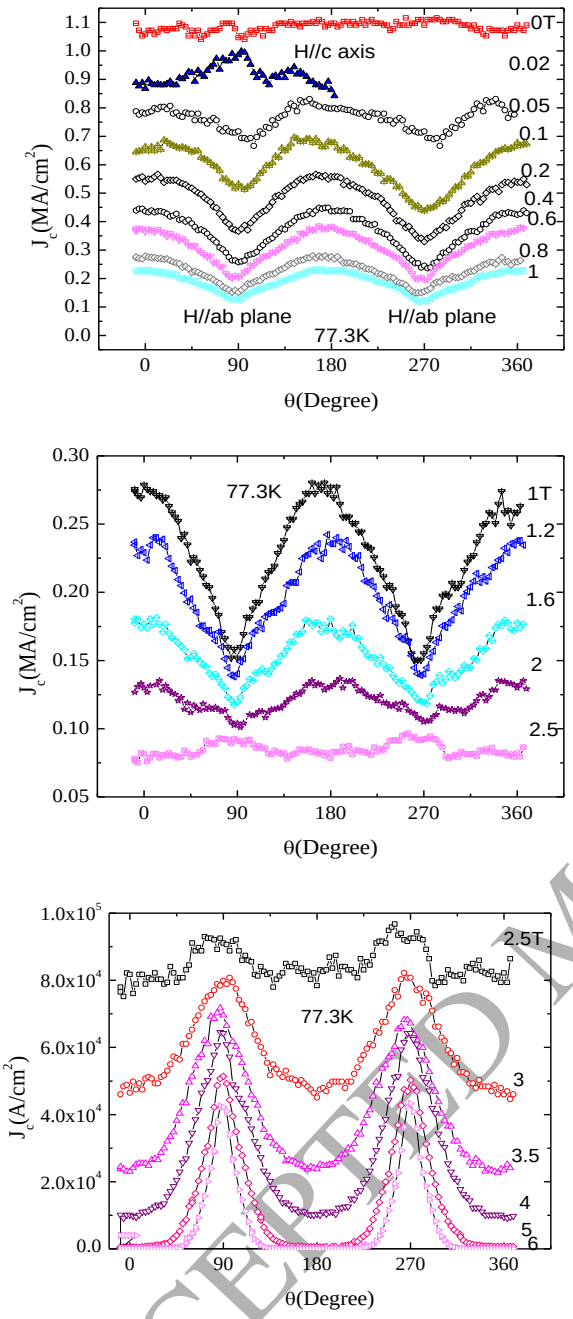

Fig. 27. Angle dependence of critical current density at 77.3 K and various fields indicated in graphs (from 0 to 1 T, top panel; from 1 T to 2.5 T, middle panel; and from 2.5 T to 6 T, bottom panel) for the BZO-doped YBCO film grown at 800^{o} C and 3 Hz.

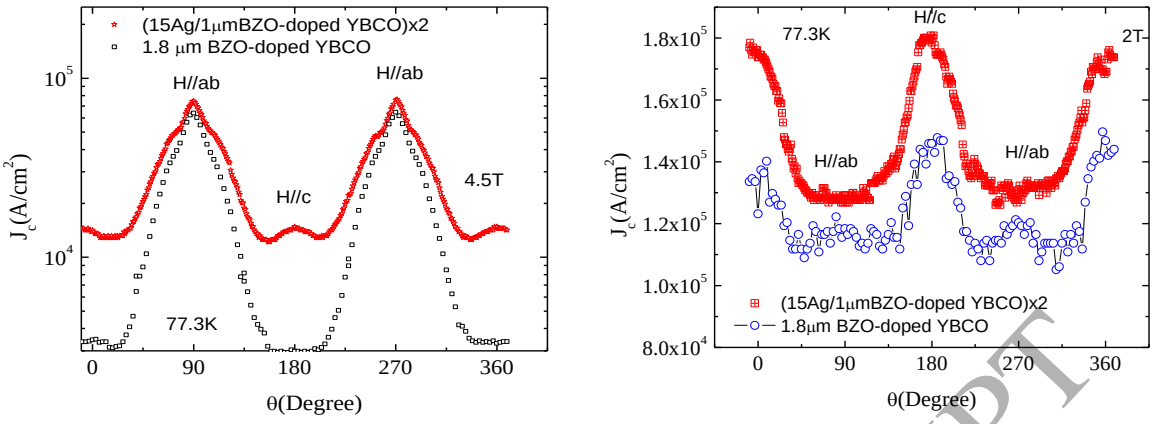

Fig. 28. Angular dependence of J_c of a (15Ag/1μm BZO-doped YBCO)x2 film and, for comparison, of a 1.8μm BZO-doped YBCO film at 77.3 K, in an applied field of 4.5 T (left-hand side) and, respectively, 2 T (right hand side). Note the fact that the film containing Ag is also slightly thicker.

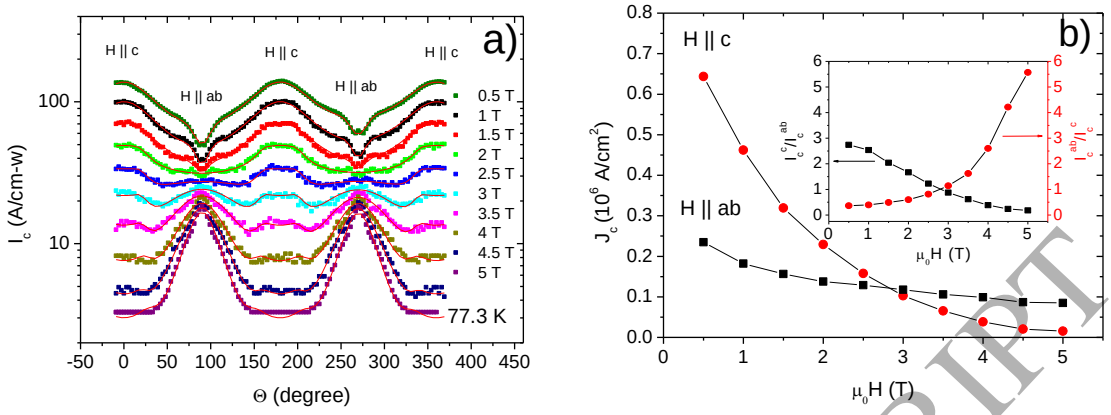

Fig. 29. a) Angle dependence of the critical current for a single-layer Ag/BZO-doped YBCO film in various fields from 0.5 to 5 T. Full lines represent the fit with the Long model. b) Field dependence of the critical current density for field parallel and perpendicular to the *a-b* plane. The insert in Fig. 29b shows the ratios of the critical current densities for the two field orientations.

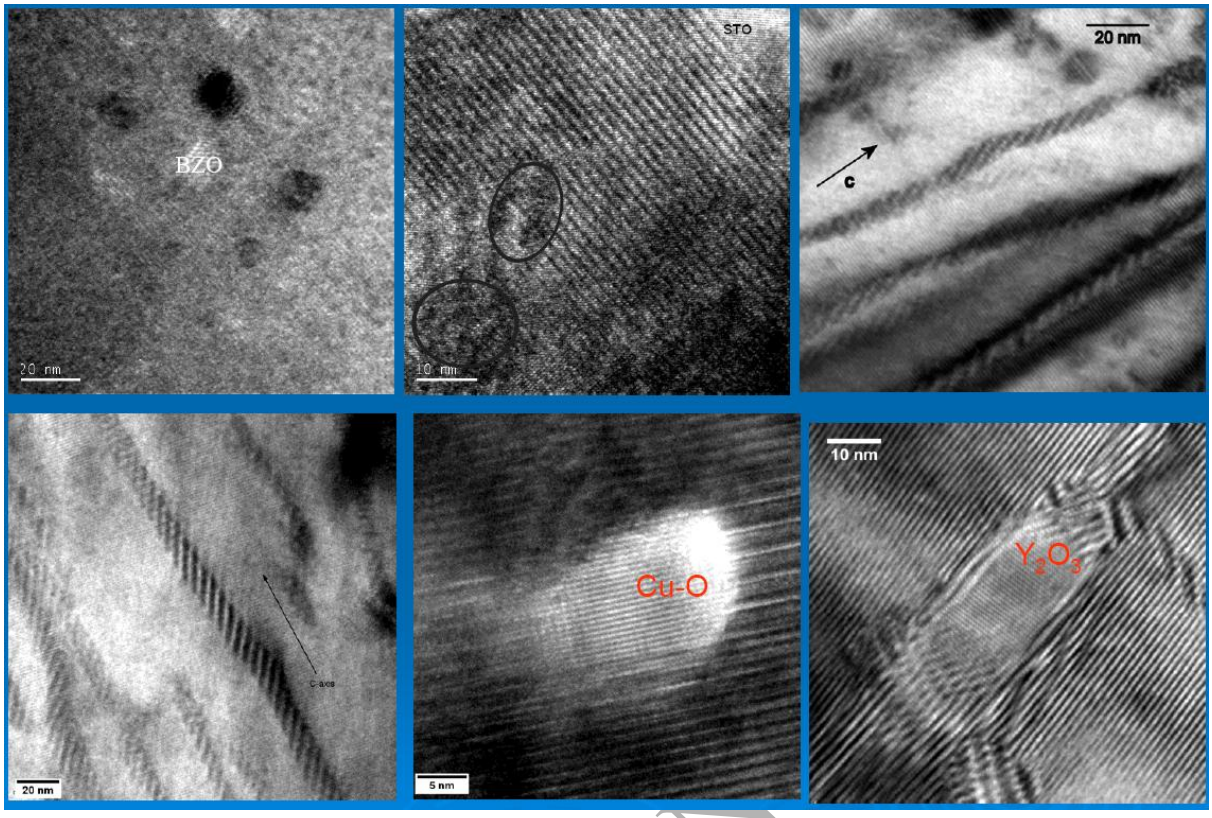

Fig. 30. TEM images showing various types of defects/pinning centres (from left to right and top to bottom): $BaZrO_3$ nanoparticles in films grown at 780^o C (first two panels); $BaZrO_3$ nanoparticles and nanorods (black arrow represent the c-axis direction) in films grown at 800^o C (third and fourth panels); Cu-O and Y_2O_3 nanoparticles (last two panels).

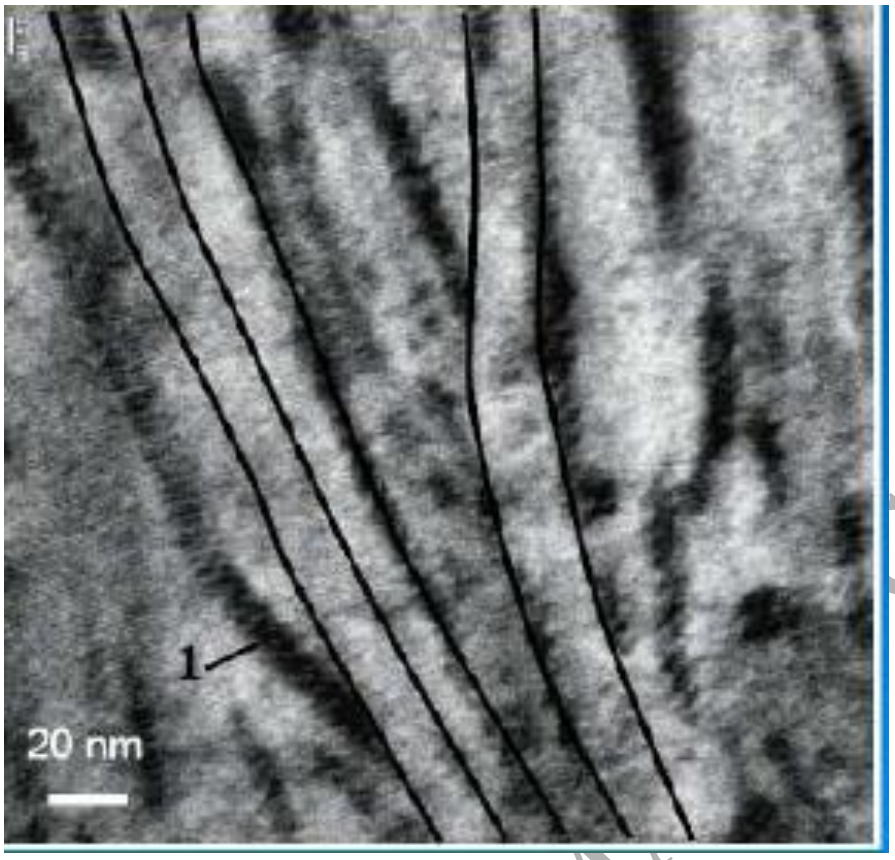

Fig. 31. $BaZrO_3$ nanorods (dark-grey) entangled with columns of YBCO (light-grey) due to Ag-induced columnar growth of YBCO. Thin black lines are guide to the eye marking YBCO columns.

Geometry of pin	Type of centre	Pinning Function	p and q values	Position of Maximum	Maximum constant
Volume	Normal	$A(1-h)^2$	p = 0; q = 2	No Max	A = 1
	Δκ	$Bh^1(1-h)^1$	p = 1; q = 1	h = 0.5	B = 4
Surface	Normal	$Ch^{1/2}(1-h)^2$	p = ½; q = 2	h = 0.2	C = 3.5
	Δκ	$Dh^{3/2}(1-h)^1$	p = $^3/_2$; q = 1	h = 0.6	D = 5.37
Point	Normal	$Eh^1(1-h)^2$	p = 1; q = 2	h = 0.33	E = 6.76
	Δκ	$Fh^2(1-h)^1$	p = 2; q = 1	h = 0.67	F = 6.76

Table 1. Reduced-field dependence of normalized bulk pinning force for various types of pinning centres.